Journal of Molecular Liquids 403 (2024) 124830

Contents lists available at ScienceDirect

Journal of Molecular Liquids

journal homepage: www.elsevier.com/locate/molliq

Impact of nanoconfinement on the physical state and conductivity mechanisms of a 2-picolinium ionic liquid crystal

Andreia F.M. Santos [a], M. Teresa Viciosa [b], Inês Matos [a], João C. Sotomayor [a], João L. Figueirinhas [c], Maria H. Godinho [d], Luis C. Branco [a], C.J. Dias [d,*], Madalena Dionísio [a,*]

[a] LAQV-REQUIMTE, Department of Chemistry, NOVA School of Science and Technology, NOVA University of Lisbon, Caparica, Portugal
[b] Centro de Química Estrutural, Instituto Superior Técnico, University of Lisbon, Lisbon, Portugal
[c] CeFEMA and Department of Physics, Instituto Superior Técnico, University of Lisbon, Lisbon, Portugal
[d] i3N/CENIMAT, Department of Materials Science, NOVA School of Science and Technology, NOVA University of Lisbon, Caparica, Portugal

ARTICLE INFO

Keywords:
Ionic liquid crystals
Confinement
Dielectric Relaxation Spectroscopy
Ionic conductivity
Charge migration mechanisms
Nyquist plots and circuits

ABSTRACT

Hybrid solid-like materials prepared from the incorporation of liquid-like ionic conductors into nanoporous matrices could represent an advantage for a variety of electronic applications. Aiming to obtain such materials, three composites of the polymorphic ionic liquid crystal (ILC) 1-hexadecyl-2-methylpyridinium bromide ([C_{16}-2-Pic][Br]), loaded in the mesoporous inorganic silica SBA-15 (~6.8 nm in pore diameter), were prepared at guest–host weight fractions of ~ 40, 60 and 80% (w/w) and investigated by different techniques: ATR-FTIR, BET, TGA, XRD and DSC. Complete amorphisation was achieved for the 40 and 60% composites, while the 80% preparation was stabilised in the low-*T* morph of native C_{16}, being in the liquid state at room temperature. Furthermore, through Dielectric Relaxation Spectroscopy, the ionic conductivity of the three hybrid materials was characterised, allowing to deconvolute this property in a pure ohmic contribution (conductivity I) and the overlapping of *ac* − *dc* transition with interfacial polarisation resulting from the coexistence of the ionic liquid and the quasi-insulating inorganic matrix (conductivity II). From –20 to 20 °C, the conductivity and the corresponding charge migration are faster in all composites relative to the neat ILC, as deduced from the inferior radii of Nyquist arcs. The 60% preparation stood out from the other materials, exhibiting direct conductivity unaffected by electrode polarisation over a larger *T*-range, leading to the assumption of a nearly continuous silica-mediated charge migration pathway, which is never reached for the 40% composite, while, in the 80% preparation, some C_{16} deposits on the outer surface of the pores. Incorporation into the silica matrix proved to be a good strategy for the production of cost-efficient materials with long-term stabilisation of the ionic liquid in a single phase over a large range of temperatures, enabling the prediction of flow and conductive properties.

1. Introduction

In a previous study by some of us [1], the conductive behaviour of *n*-alkyl-2-picolinium bromide [C_n-2-Pic][Br] ionic liquids (ILs) was investigated. ILs with $n = 12$ and 16 turned out to be ionic liquid crystals (ILCs) that undergo conversion between polymorphs, as well as crystal to liquid crystal transition and isotropisation. The multiplicity of phase transitions may represent a disadvantage when these emerge at operating temperatures. Aiming to solve this issue, deposition on a surface can be used as a strategy to stabilise the material in a different phase other than the most stable one. This surface mediated effect was observed for materials with interest in electronics [2] and optoelectronics [3], as well as in active pharmaceutical ingredients (APIs) [4]. Furthermore, encapsulation within pores at a nanometric scale allows the guest to be retained in a single phase, as a metastable polymorph, which is the case for a perovskite [5] and some APIs [6,7]. Ultimately, incorporation inside a nanostructured matrix may fully prevent crystallisation and the guest is stabilised in a structurally disordered amorphous material [8]. The introduction of disorder could enhance conductivity [9–11], providing new pathways to charge migration across interfaces [12,13], with the beneficial of homogeneous expansion and contraction of the material in the case of electrodes [14]. However, it could also hamper the ionic transport by interrupting fast charge migration pathways [15]. Therefore, the impact of introducing

* Corresponding authors.
E-mail addresses: cmd@fct.unl.pt (C.J. Dias), madalena.dionisio@fct.unl.pt (M. Dionísio).

https://doi.org/10.1016/j.molliq.2024.124830
Received 12 December 2023; Received in revised form 4 April 2024; Accepted 24 April 2024
Available online 26 April 2024

disorder and defects is unclear, although it has already been established that their extension allows to tune the ionic conductivity [16]. In this context, the present work explores the incorporation into a mesoporous silica matrix as a strategy to build a hybrid material that retains the ionic liquid crystal [C_{16}-2-Pic][Br] in a single phase to fulfil the increasing demand for solid electronic devices with improved performance at room temperature [17,18]. The need for silica loading arises from the fact that the target material undergoes polymorphic transitions between –10 and 50 °C, a range that includes the usual working temperatures, with the disadvantage that their exact location in temperature depends on the cooling/heating rate. Additionally, incorporation into the pores may prevent reversion to the original state, as observed for other ionic conductors after mechanical induction of disorder by ball milling [19] and also in a long-term stabilisation of otherwise unstable forms [20].

The mesoporous silica SBA-15 was chosen to host [C_{16}-2-Pic][Br], being obtained by using an amphiphilic block copolymer as organic structure directing agent [21]. It exhibits a well-ordered hexagonal array of pores, whose diameter can be tuned during synthesis by the appropriated choice of the alkyl chain length of the surfactant [22], making it possible to tailor the material to suit specific applications. These materials have found uses in many fields of interest, such as catalysis [23], environmental remediation [24,25], biochemistry [26], drug delivery [27–29] and, more recently, electronics [30], since the high surface area and large pore volume, resulting in high loading capacity, as well as the narrow pore size distribution and ordering at a nanometric scale, represent an advantage for the control of charge transport [30], increasing proton conductivity [31], ionic transport [32], energy and power density, exhibiting improved lifetime and stability [33]. Moreover, the volatility and flammability of high power density materials [34] is reduced upon incorporation inside such thermal resistant hosts [35,36]. In fact, confinement into a porous matrix makes it possible to obtain an enhanced solid-type electrolyte [37], as, if the charged material is kept in the liquid state, either supercooled or isotropic liquid, it is possible to overcome the disadvantages of solid electrolytes arising from their high internal impedance [38].

Aiming to evaluate the feasibility of a solid-type material with interest for electronic applications, [C_{16}-2-Pic][Br] was loaded into SBA-15 at three different guest-to-host weight ratios: 40%, 60% and 80% (w/w). After preparation, the hybrid materials were investigated by a set of experimental techniques to confirm loading (Thermogravimetric Analysis (TGA), Porosimetry (BET), Attenuated Total Reflectance Fourier Transform Infrared (ATR-FTIR)), to access the guest physical state (X-Ray Powder Diffraction (XRD)) and Differential Scanning Calorimetry (DSC)) and, finally, to characterise their ionic conductivity (Dielectric Relaxation Spectroscopy (DRS)) from which the equivalent electrical circuit is derived. Moreover, the composites' conductivity near room temperature was compared with the bulk ILC and discussed in terms of guest physical state and silica-assisted charge migration pathways.

2. Experimental part

2.1. General remarks

All commercial organic solvents were purchased from different chemical companies. 2-Picoline (Solchemar, 98% purity) and 1-bromohexadecane (Aldrich, 97% purity) were used as received without further modifications. Tetraethyl orthosilicate (TEOS, 98% purity) and poly (ethylene)glycol-*block*-poly(propylene)glycol-*block*-poly(ethylene)glycol (P123) were supplied by Aldrich.

2.2. Synthesis of starting materials

1-Hexadecyl-2-methylpyridinium bromide, [C_{16}-2-Pic][Br], was previously synthetised and chemically characterised [1]. Table 1 comprises some information regarding the starting ILC. The mesoporous silica was prepared following an adapted procedure based on the literature [39]. To obtain the desired pore size (6.8 nm), 2 g of triblock copolymer P123, as structure–directing agent, was dissolved in 15 mL of deionised water and 60 mL of a 2 M HCl solution, followed by the addition of 4.4 g of the silica source, TEOS, dropwise at room temperature. The obtained solution was stirred for 24 h at 40 °C and, then, transferred to a Teflon-lined autoclave at 100 °C for another 24 h. The resulting precipitate was filtered, washed with deionised water and dried. The final SBA-15 was obtained after calcination at 500 °C in air for 5 h to remove the template.

Table 1
Chemical structure, molar mass, physical state and geometrical parameters of [C_{16}-2-Pic][Br].

	[C_{16}-2-Pic][Br]
Chemical structure	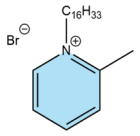
Molar mass (g mol^{-1})	398.47
Physical state	Polymorphic crystal
Cation size[a] (Å)	25.007
VdW diameter[b] (Å)	26.94

[a] Cation size estimated by Avogadro molecular modelling software (version: 1.2.0).
[b] Van der Waals diameter determined for the cation longer radius, which was assessed by MarvinSketch software (version: 22.11.0). Regarding bromide, the diameter was calculated from the correspondent VdW volume (26.5 Å^3) [40].

2.3. Loading into mesoporous silica matrix

To eliminate water and other volatile impurities, which could be contained in the pores of the SBA-15 mesoporous silica, ~ 150 mg of silica were vacuum-degassed (10^{-4} bar) at 150 °C for 8 h. The temperature of the glass silica container was assured by an electric cylindrical oven. After this period, the silica container was allowed to cool down to room temperature. Then, a solution of ~ 40, 90 or 120 mg of [C_{16}-2-Pic][Br] dissolved in 4 mL of chloroform was transferred to the glass cell containing the silica matrix under vacuum, after which the solvent was slowly evaporated under gentle stirring for three days at room temperature and a dry powder was recovered. The obtained hybrid materials were designated as C_{16}@SBA_40%, C_{16}@SBA_60% and C_{16}@SBA_80%, in weight percentage (w_{C16}/w_{silica}). For comparison purposes, [C_{16}-2-Pic][Br] was also incorporated in a MCM-41 matrix (3.5 nm in pore size), named as C_{16}@MCM_60% (see the respective physical characterisation in Figure S1 in ESI).

2.4. Characterisation of composites

Porosimetry (BET): N_2 adsorption–desorption isotherms at –196 °C were acquired on an ASAP 2010 V1.01B Micromeritics equipment at Analysis Laboratory of LAQV-REQUIMTE, Chemistry Department, NOVA School of Science and Technology, Portugal. Apparent surface area (S_{BET}) was determined using Brunauer-Emmett-Teller (BET) equation, while total pore volume was determined by the amount of nitrogen adsorbed at the relative pressure $P/P_0 = 0.95$. Pore diameter and volume were calculated from Barret-Joyner-Halenda (BJH) in the desorption branch and Density Functional Theory (DFT) methods, respectively.

Thermogravimetric Analysis (TGA): The degradation profile of the materials was monitored from 33.50 to 500 °C in a Thermogravimetric Analyser from Setaram Labsys EVO with weighing precision of ± 0.01%. Each run was conducted at a heating rate of 5 °C min^{-1}, under a highly pure argon atmosphere purged at 50 mL min^{-1}, with a mass sample

between 9 and 10 mg.

Attenuated Total Reflectance Fourier Transform Infrared Spectroscopy (ATR-FTIR): Attenuated Total Reflectance Fourier Transform Infrared Spectroscopy spectra were carried out on a PerkinElmer Two FT-IR Spectrometer equipped with a universal attenuated total reflectance sampling accessory. The respective spectra were obtained through Spectrum 10 software, also from PerkinElmer, and the samples were analysed in the 400 − 4000 cm^{-1} spectrum range.

X-Ray Powder Diffraction (XRD): X-Ray scattering profiles were acquired at room temperature, using a variable geometry setup equipped with a Max-Flux Optic graded multilayer monochromator (CuKa radiation: λ = 1.54056 Å) and an INEL CPS 590 gas curved detector in association with a computer-controlled data acquisition system. The apparatus acquisition system was calibrated using the scattering peaks of a Silver Behenate sample.

Differential Scanning Calorimetry (DSC): Thermal studies were carried out using a DSC Q2000 from TA Instruments Inc. (Tzero DSC technology) coupled to RCS 90 cooling system and operating in the Heat Flow T4P option. Measurements were performed under anhydrous conditions purged with 50 mL min^{-1} of high purity nitrogen flow. DSC Tzero apparatus calibration was done in the temperature range between –90 and 200 °C. Enthalpy (cell constant) and temperature calibration were based on the melting peak of indium standard (T_m = 156.60 °C) supplied by TA Instruments (lot number: E10W029). For each experiment, ~3 − 9 mg of sample were weighted and encapsulated in a hermetic Tzero aluminium pan and lid. All capsules were sealed before the analysis and the respective lids were perforated to avoid the pressure increase due to water evaporation. The experimental procedure consisted of first equilibrate all samples at 20 °C followed by cooling to –90 °C and heating up to 80 °C, keeping the sample 20 min at this temperature to cause water evaporation. Then, the sample was submitted to two successive cooling and heating runs between –90 and 160 °C carried at 10 °C min^{-1}. To better disclose the glass transition, temperature modulated DSC (TMDSC) was performed from –60 to 80 °C, using the oscillation periods 60, 80 and 100 s, with the respective amplitudes 0.32, 0.42, 0.53 °C, at a heating rate of 0.5 °C min^{-1}. At the end of each modulated segment, the sample was heated up to 140 °C to melt any possible crystalline fraction. The glass transition was obtained from the heat capacity reversing signal. Data treatment was carried out through Universal Analysis 2000 software by TA Instruments Inc.

Dielectric Relaxation Spectroscopy (DRS): For the dielectric measurements, performed in an ALPHA-N impedance analyser from Novocontrol Technologies GmbH, the powder sample was sandwiched between two gold plated electrodes (10 mm in diameter) in the BDS 1200 sample cell. Moreover, two silica spacers (50 μm in thickness) were used to avoid short-circuit and to assure constant thickness. The sample cell was placed in a cryostat (BDS 1100) and the temperature control was assured by the Quatro Cryosystem with an uncertainty ± 0.5 °C. Firstly, samples were submitted to a pre-treatment up to 160 °C to remove adsorbed water. Spectra, scanned over a frequency range from 10^{-1} to 10^{6} Hz, were isothermally acquired from –110 to 160 °C, in steps of 5 °C, except in the region between –40 and 50 °C in which the acquisition was every 2 °C.

Dielectric Relaxation Spectroscopy data treatment: In DRS, the material is submitted to an outer electrical field that causes a preferential alignment of internal dipoles, designated orientational polarisation. However, this dielectric response does not develop instantaneously due to viscosity, a measure of the fluid resistance acting against dipole reorientation. Also, when the electric field is removed, as in static measurements, the loss of alignment is not instantaneous. Instead, there is a time-dependent loss of dipole orientation, called dipolar relaxation. In dynamic measurements, a frequency-variant electric field is applied causing a phase lag between the applied oscillating stimulus and the resulting orientational polarisation, which is mathematically described by the formalism of complex numbers [41]. DRS measures then a complex permittivity as a function of angular frequency, $\varepsilon^*(\omega) = \varepsilon'(\omega)\text{-}i\varepsilon''(\omega)$, whose real, $\varepsilon'(\omega)$, and imaginary, $\varepsilon''(\omega)$, components are associated, respectively, with the energy stored and dissipated by the material; the latter is due to dipoles unable to follow the oscillating field. If a relaxation process is being probed, the real component follows a sigmoidal profile, while the imaginary one is bell-shaped, corresponding to the logarithmic derivative of the former, both being related by Kramers-Kronig transforms [42,43]. The analysis of the isothermal complex permittivity is usually made through the Havriliak-Negami (HN) model function [44,45]. Nevertheless, when data are greatly affected by conductivity, as in the case of the present investigation that deals with ionic species, it could be advantageous to analyse the complex electrical modulus, $M^*_{HN}(\omega)$, defined as the reciprocal of the complex permittivity: $M^*(\omega) = 1/\varepsilon^*(\omega)$ [41,46]. The ionic conductivity appears as a peak in the imaginary modulus component, facilitating the conductivity analysis and allowing a better resolution between dipolar relaxation and conduction relative to ε'' [47].

In the present work, isothermal conductivity spectra were analysed through Jonscher equation (Equation (1)) [48]:

$$\sigma'(f) = \sigma_{dc}\left[1 + \left(\frac{f}{f_{cross}}\right)^{s}\right] \quad (1)$$

where σ_{dc} is the direct current conductivity estimated from the range where the conductivity is frequency independent, s ($0.5 \leq s \leq 1$) is a material and temperature dependent parameter, meaning pure ohmic conductivity if $s = 1$ [46], and f_{cross} the linear frequency at which the plateau bends off, separating the semi-diffusive (*ac*) and diffusive (*dc*) regimes.

In electrical modulus representation, and when a multimodal profile is found, a sum of HN-type functions is considered to fit the acquired modulus spectra, identical to what is used to simulate the complex permittivity [46,47], here expressed in function of linear frequency, f.

$$M^*_{HN}(f) = M_\infty + \sum_{j=1}^{n} \frac{\Delta M}{\left(1 + \left(-i\left(\frac{f}{f_o}\right)^{-1}\right)^{\alpha_{HN}}\right)^{\beta_{HN}}} \quad (2)$$

In Equation (2), j is the index over which the individual n processes are summed. $\Delta M = M_\infty - M_o$ [49], while α_{HN} and β_{HN} are shape parameters ($0 < \alpha_{HN} < 1$ and $0 < \alpha_{HN}.\beta_{HN} \leq 1$), describing, respectively, the symmetric and asymmetric broadening of the complex electric function [46]. The simulation of the experimental imaginary component of M* was carried out using the software *Grafity* (GrafityLabs). From the frequency obtained by the fit (f_0), a model independent f_{max} is estimated according to Equation (3) [44]:

$$\frac{1}{f_{max}} = \frac{1}{f_0}\left[sin\left(\frac{\alpha_{HN}\pi}{2+2\beta_{HN}}\right)\right]^{\frac{1}{\alpha_{HN}}}\left[sin\left(\frac{\alpha_{HN}\beta_{HN}\pi}{2+2\beta_{HN}}\right)\right]^{-\frac{1}{\alpha_{HN}}} \quad (3)$$

that allows to extract the characteristic relaxation time, $\tau_{M'}$, as $\tau_{M'} = (2\pi f_{max})^{-1}$. To further describe $\tau_{M'}$ temperature dependence, the Vogel-Fulcher-Tammann-Hesse (VFTH, Equation (4)) law [50–52] was used

$$\tau_{M'}(T) = \tau_\infty \exp\left(\frac{B}{T - T_0}\right) \quad (4)$$

where τ_∞ is the relaxation time at the high temperature limit, B is inversely related to the deviation from linearity of the plot (roughly, higher curvatures correspond to lower B values) and T_0 is the absolute Vogel temperature.

3. Results and discussion

3.1. Evidence of guest loading

In order to get evidence that [C_{16}-2-Pic][Br] was successfully loaded in the mesoporous silica, the prepared hybrid materials were submitted

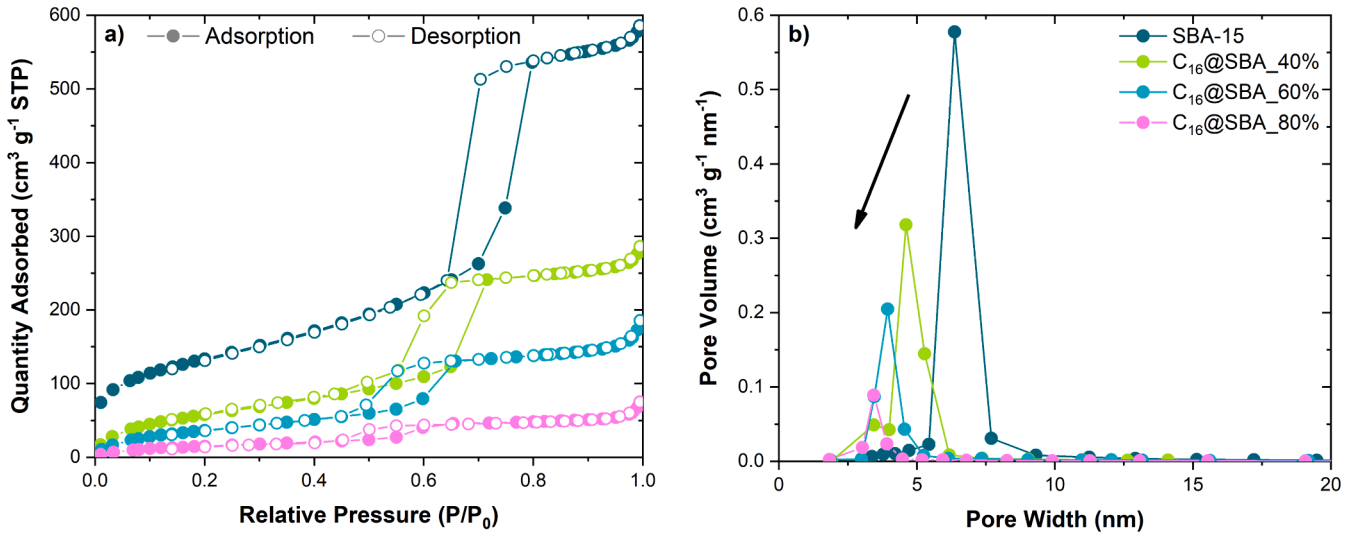

Fig. 1. Porosimetric analysis for the unloaded SBA-15 (darker circles) and the three composites: a) nitrogen adsorption/desorption and b) pore size distribution (desorption branch), showing the decrease of pore average with the increase amount of C_{16} (arrow).

to Porosimetry (BET, Fig. 1) and Thermogravimetry (TGA, Fig. 2) analyses to evaluate the pore size and distribution as well as the weight loss profile and percentage of loading.

Textural studies were carried out by nitrogen sorption for both matrices before and after loading. The N_2 adsorption (full symbols) and desorption (open symbols) isotherms obtained for the unloaded matrix is shown in Fig. 1a. According to the most recent IUPAC classification [53], the obtained profile can be assigned to type IV(a) physisorption isotherms, characteristic of mesoporous materials. Moreover, the observed hysteresis loop originated by capillary condensation is coherent with H1 type, consistent with pore ordered structure and narrow mesopores size distribution [54], as illustrated in Fig. 1b for the synthesised SBA-15 and composites. After loading, nitrogen adsorption volume decreases as the C_{16} content increases. However, the isotherm type IV(a) is preserved along with the hysteresis loop H1 (see Fig. 1a). This indicates that the mesoporous structure of the silica is maintained and suggests that the incorporation of the guest occurs within the pores, reducing the volume available for nitrogen adsorption. Furthermore, the closure point of the hysteresis loop occurs at decreasing relative pressures upon [C_{16}-2-Pic][Br] increase, compatible with a reduction of pore diameter [55,56]. This is confirmed by the shift to lower values of the pore size distribution with increasing loading, as shown in Fig. 1b, reinforcing that the incorporation of the guest took place inside the pores. Since the overall salt dimensions are determined by the cation size (2.5 nm) and Van der Waals diameter (2.7 nm) (Table 1), which are smaller than the pore diameter (see Table 2), incorporation was expected to occur within the pores. A different scenario was observed for C_{16} loaded in another silica matrix (Figure S1a), MCM-41 type, with inferior pore diameter (3.5 nm). This pore dimension is much closer to the length of C_{16}, whose isotherm reveals almost no nitrogen uptake due to pores occlusion [57–59].

Moreover, an initial concave rise is observed in the adsorption–desorption isotherms of the unloaded silica at the low relative pressure region due to micropore filling [60]. This effect is almost absent in the loaded matrices, indicating that micropores are inaccessible for N_2 molecules due to prior ILC adsorption.

The loaded C_{16} amount was quantified by Thermogravimetric Analysis. Fig. 2 displays the obtained thermograms. While no mass loss

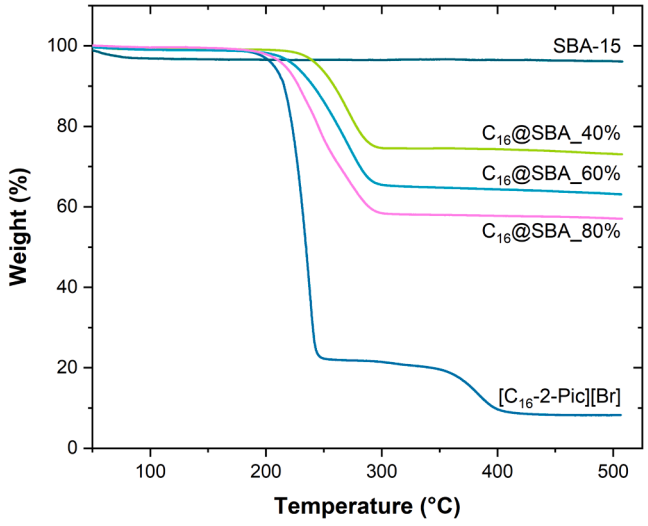

Fig. 2. Thermogravimetric curves obtained on heating at 5 °C min^{-1} for the unloaded SBA-15 and the three composites. Neat C_{16} is included for comparison.

Table 2
Textural parameters obtained from BET, BJH and DFT methods for unloaded and loaded SBA-15.

	Surface area (m^2 g^{-1})	Pore diameter (nm)	Pore volume (cm^3 g^{-1})	Loading % (w/w)
SBA-15 (unloaded)	483	6.84	0.78	–
C_{16}@SBA-15_40%	226	5.42	0.42	35.8
C_{16}@SBA-15_60%	145	5.36	0.27	56.7
C_{16}@SBA-15_80%	59	5.59	0.08	74.4

For all materials, the specific surface area was determined from the linear portion of the Brunauer-Emmett-Teller (BET) plots, whereas pore diameter and volume were calculated from Barret-Joyner-Halenda (BJH) desorption and Density Functional Theory (DFT) methods, respectively. The percentage of loading was estimated by Thermogravimetric Analysis (TGA).

is observed for the pristine matrix, except a small decrease up to 150 °C due to water desorption (4% w/w), the neat ionic liquid starts to decompose above 170 °C [1]. The thermal resistance increases by loading C_{16} into SBA-15, as the onset of degradation shifts towards higher temperatures with the increase amount of silica matrix. The loading percentage in each composite was estimated from the mass loss after discount the adsorbed water (~1%), closely agreeing with C_{16} and SBA-15 amounts used in the starting preparations (see the last column of Table 2). Therefore, the rounded designation 40, 60 and 80% (w/w) was adopted.

These techniques confirmed the presence of guest in all hybrid materials, evidence that was also provided by Attenuated Total Reflectance Fourier Transform Infrared Spectroscopy (ATR-FTIR, Figure S2) by comparing the spectra of the composites with those of neat ILC and empty matrix. In the latter, the siloxane framework exhibits the Si−O−Si asymmetric stretching vibration mode at 1071 cm^{-1}, with a high wavenumber shoulder at 1139 – 1240 cm^{-1}. The respective bending is detected at 444 cm^{-1}. The bands registered at 968 and 806 cm^{-1} are attributed to Si−OH vibrations in the silanol moieties and symmetric stretching vibrations of Si−O−Si, respectively [61–63]. For the composites, these bands still dominate the spectra, although the C−H stretching modes of the C_{16} alkyl tail (2918 and 2851 cm^{-1}) and the C=C−C stretch of the aromatic ring (1633, 1516 and 1465 cm^{-1}) are also detected (highlighted areas in Figure S2), confirming the presence of [C_{16}-2-Pic][Br].

Table 2 summarises the textural parameters obtained from the porosimetric analysis and the percentage of loading calculated by the weight loss profile of each hybrid material.

3.2. Physical state of loaded C_{16}

To access the physical state of loaded C_{16}, the three incorporations were submitted to X-Ray Powder Diffraction (XRD, Fig. 3) and Differential Scanning Calorimetry (DSC, Fig. 4).

Concerning XRD analysis, the collected diffractograms are presented in Fig. 3. For neat [C_{16}-2-Pic][Br], at room temperature, a Bragg diffraction pattern is obtained, characteristic of an ordered crystalline structure. On contrary, the XRD pattern registered for the pristine SBA-15 matrix in the scanned 2θ range only shows peaks relative to long-distance order of the two-dimensional hexagonal arrays of SBA-15 mesopores at lower angles (2θ < 2°), being more accurately detectable by Small-Angle X-Ray Diffraction [64–66]. The lack of Bragg peaks at higher 2θ values (2θ > 10°) for the pristine matrix is indicative of SBA-15 amorphous nature. For all composites, only the SBA-15 low angle peaks are reproduced, confirming the structural invariance of the silica matrix upon loading and the absence of a C_{16} crystalline component. The [C_{16}-2-Pic][Br] amorphisation points to a guest incorporation inside pores. For the highest concentration sample (80%), a longer XRD acquisition was performed in search of any residual ILC fraction deposited outside the pores. Although no evidence supporting this hypothesis was obtained using this technique, it was provided by calorimetry, as will be discussed next.

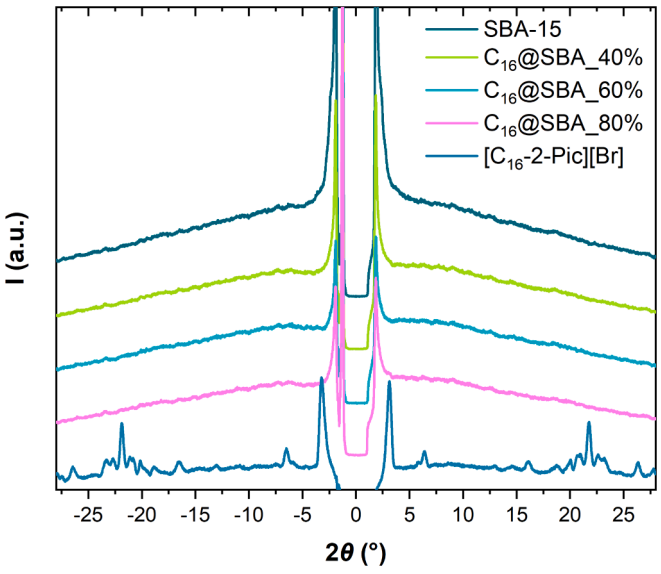

Fig. 3. Diffractograms obtained for the unloaded SBA-15 matrix the three composites compared with the crystalline pattern of neat C_{16}. The long-distance order of the matrix gives rise to peaks detected below 3°, while the absence of Bragg peaks at higher 2θ values confirms its amorphous nature, a spectral signature that is preserved in the composites.

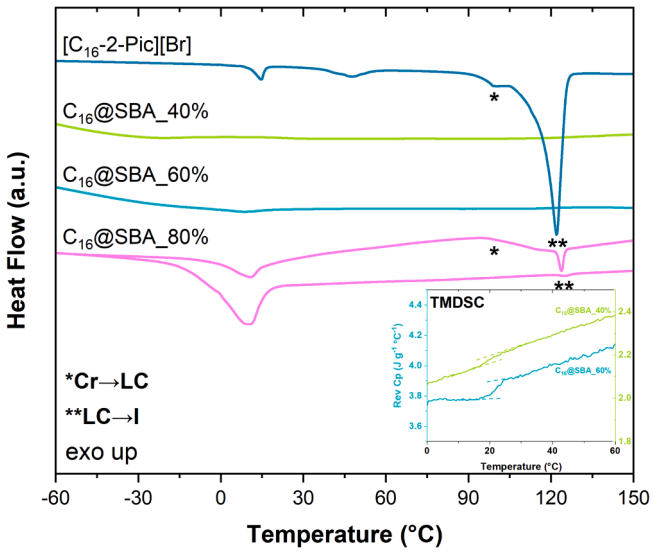

Fig. 4. Comparison of the thermograms obtained for the second heating run of [C_{16}-2-Pic][Br], C_{16}@SBA_40%, C_{16}@SBA_60% and C_{16}@SBA_80%, all carried out at 10 °C min^{-1}. For the latter, a scan at higher rate (30 °C min^{-1}) is provided to show the enhancement of the low-*T* morph endotherm upon thermal cycling. The inset presents the sinusoidal temperature variation of TMDSC cooling runs, performed at 0.5 °C min^{-1}, disclosing the glass transition steps of C_{16}@SBA_40% and C_{16}@SBA_60%.

To gain additional insights into the physical state of [C_{16}-2-Pic][Br] after being loaded in SBA-15, the different materials were submitted to calorimetric analysis, being the thermograms represented in Fig. 4. After an initial heating to 80 °C, where samples were held isothermally for 20 min to remove water adsorbed by the hydrophilic silica matrix, the materials were cooled down to –90 °C and subsequently heated up to 160 °C. The final temperature was chosen to evaluate if the transition to the liquid crystalline phase (Cr → LC ~ 100 °C) and isotropisation (LC → I ~ 124 °C), detected in neat [C_{16}-2-Pic][Br] [1], also occur in the hybrid materials.

For C_{16}@SBA_80%, the respective DSC curves show that, although with rather small magnitudes, those bulk-like transitions are observed at nearly the same temperatures (see asterisks). If crystallisation took place inside the pores, a depression of the melting point would be expected. In fact, for confinement sizes comparable to the critical size for crystal growth, a decrease in melting temperature is predicted according to the Gibbs-Thomson equation [67], as observed for several low molecular weight guests [68–74] and confined water [75]. This effect was not detected in the 80% compound, corroborating the assumption that, at least, a small fraction of C_{16} is deposited outside the pores. The observation of an unchanged melting temperature was also found for C_{16} loaded in MCM-41 (Figure S1d), a lower pore size matrix, for which, the respective BET adsorption–desorption isotherms (remember Figure S1a) are characteristic of a completely or partially filled matrix with blocked pores. In this MCM-41 composite, the bulkiness of C_{16} impairs the

entrance in the small pores, leaving a fraction of material on the outer surface, which melts at the same temperature of the neat ILC. Likewise, also in the 80% hybrid material, some ILC remains on the outer surface of SBA-15. Nonetheless, the small enthalpy value (<1 J g^{-1}) associated with the melting of C_{16}@SBA_80% indicates a residual crystalline component that was not distinguished by XRD, even in a long run diffractogram. Furthermore, a crystallisation/melting near above 0 °C, in both cooling and heating runs, is clearly detected for C_{16}@SBA_80%. It is worth to note that the two weak bulk-like transitions already referred progressively fade away from the DSC curve upon thermal cycling, probably due to migration of the molten liquid to inside pores (remember the corresponding BET isotherm in Fig. 2 that still allows a minor fraction to enter). On the other hand, the transition associated with crystallisation and melting of the low-*T* morph becomes more pronounced (see the bottom curve in Fig. 4), which seems to confirm that the respective material is located inside pores, losing its liquid crystalline nature and stabilising the lower temperature polymorph upon loading in the SBA-15 matrix. A similar surface mediated effect was observed for several materials [2,3]. Moreover, as the melting endotherm undergoes only a small depression of ~ 3 °C relative to bulk C_{16}, the associated critical radius for crystal growth of this low-*T* morph must lye below or be in the same order of the pore diameter [76]. A possible arrangement may consist of cations lying with their long alkyl tails parallel to the pore axis, preventing the layered organisation of the smectic mesophase found in pure C_{16} and justifying the suppression of liquid crystalline behaviour. Even more, when the 80% composite is analysed through TMDSC, the intermediate polymorph calorimetrically observed at ~ 50 °C in neat C_{16} is also resolved at such low heating rate (0.5 °C min^{-1}, Figure S3). It cannot be completely ruled out, due to the similarity of the endotherms profile between C_{16}@SBA_80% and [C_{16}-2-Pic][Br], that the polymorphs disclosed for the composite at ~ 0 and 50 °C in TMDSC experiments correspond to significant downwards shifts of the melting of the bulk-like intermediate morph (50 °C) and conventional crystal (124 °C) of neat ILC.

Oppositely to what occurs in C_{16}@SBA_80%, no signs of a bulk-like melting were detected for C_{16}@SBA_40% and C_{16}@SBA_60%, leading to conclude that, in both hybrid materials, all the guest is incorporated inside pores. Therefore, a suppression of the guest's liquid crystalline to the isotropic phase transition occurs for the three preparations, in line with was reported for other ILCs [77]. Moreover, for the 40 and 60% composites, no low-*T* melting is registered and so the in-pores C_{16} fraction avoids crystallisation, which should give rise to a glass transition. However, no clear indication is provided, just a small discontinuity in the heat flow during cooling, being imperceptible upon heating. In search for a glass transition, TMDSC experiments were also performed for these two composites, as temperature modulated DSC increases both resolution and sensitivity [78]. The inset of Fig. 4 shows a scale up of the temperature region where a step of the reverse heat capacity is detected during heating at 0.5 °C min^{-1}, disclosing the signature of the glass transition in both 40 and 60% composites. The inflection points are located, respectively, at ~ 21 °C and ~ 22 °C, corresponding to the peak position of the first derivative of the reverse heat capacity signal. Hence, DSC confirms the amorphisation of C_{16} in these preparations, as previously stated through XRD analysis. Due to the high tendency to undergo crystallisation, it was not possible to detect the glass transition in neat C_{16}. However, an estimate by the empirical rule $T_g = 2/3\ T_m$ [79], which is strictly obeyed by the lower member of the series [C_6-2-Pic][Br] [1], gives a value of –8 °C. Therefore, the increased T_g in composites could be originated by a more rigid population adsorbed to the pore walls [80].

For these two hybrid materials, the multiple transitions underwent by native C_{16} are reduced only to vitrification (on cooling) and devitrification (on heating), revealing high stability against temperature changes. This was confirmed even after 12 months of incorporation. Taking into account that the material's ordering is highly dependent on the alkyl chain length [81,82], it is worthwhile to emphasise that the polymorphic ionic liquid 1-hexadecyl-1-methylpyrrolidinium bis(trifluoromethanesulfonyl)imide [C_{16}MPyrr][NTf_2] [81] always crystallise on cooling when incorporated in anodised aluminium oxide membranes with pore diameters of 10 and 80 nm. Thus, the avoidance of crystallisation in 40 and 60% composites can be seen as a manifestation of finite size effects in the 6.8 nm SBA-15 pores.

3.3. Dielectric characterisation

3.3.1. Conductivity analysis

The prepared composites were investigated by Dielectric Relaxation Spectroscopy. After a first heating ramp up to 160 °C to remove adsorbed water, spectra were collected from –100 °C to 160 °C, following the same procedure adopted for the study of neat C_{16} [1]. The real component of conductivity thus obtained is plotted in function of frequency at some representative temperatures, between –50 and 100 °C, in Fig. 5.

The universal conductivity profile found for semiconducting disordered materials is obeyed [48,83–85]. At low temperatures and/or high frequencies, a semi-diffusive region gives rise to frequency dependent (*ac*) conductivity, where charges are trapped in potential-energy valleys due to Coulombic forces of the cage-forming counter ion neighbours [86]. On the other side, long-distance translational charge migration originates a sort of plateau, meaning a frequency independent (*dc*) conductivity. For both 60 and 80% preparations, the direct current conductivity (σ_{dc}) plateau clearly emerges above 20 °C (Fig. 5c and 5d), while it is never attained for the 40% composite (Fig. 5b) due to electrode polarisation (EP). This EP effect manifests in a decrease of the conductivity at low frequencies, as charges accumulate near the electrode surface, building an interfacial layer that blocks electrical discharge [46,87]. The Jonscher law (Equation (1)) was fitted to the conductivity isotherms up to 160 °C, starting at ~ 10 °C (in the case of 60 and 80% hybrid materials) and 60 °C (for the 40% composite). Examples of such data treatment are provided in Figure S4: the *s* parameter was found to increase from 0.51 (60 °C) to 0.61 (160 °C) for C_{16}@SBA_40% and from 0.66 (~10 °C) up to 0.76 (160 °C) for the other two. Both temperature increase and range of estimated *s* values are coherent with the correspondent values found in ionic conductors [88]. The extracted σ_{dc}(T) (Figure S4d) will be analysed in the Modulus section.

Furthermore, the conductivity spectra are compared in Fig. 6a at 20 °C, illustrating the different regimes and effects. Fig. 6b and 6c comprise the dielectric response expressed in terms of real conductivity $\sigma'(f)$, imaginary electrical modulus $M''(f)$ and dielectric loss $\varepsilon''(f)$ for C_{16}@SBA_40% and C_{16}@SBA_80%.

Regarding C_{16}@SBA_80% (Fig. 6c), the respective $\varepsilon''(f)$ spectrum (circles) in a log–log plot has a conductivity tail, with a slope close to 1, at the lowest frequencies, indicating the emergence of ohmic conductivity, hereafter designated as conductivity I. This agrees with the presence of the plateau in the $\sigma'(f)$ spectra (squares). At intermediate frequencies, the $\varepsilon''(f)$ plot exhibits a lower slope in which conductivity is not strictly *dc*, henceforth mentioned conductivity II. In the modulus representation (triangles in Fig. 6b and 6c), the conductivity gives rise to a peak [46,47]. As frequency increases (10^3 – 10^4 Hz), a sort of relaxational process overlaps the conductivity for the 80% composite, converting to a peak in both $M''(f)$ and $\varepsilon''(f)$, being better resolved in the former representation. Therefore, the three properties provide evidence of such relaxational behaviour where the maximum in the modulus representation is slightly shifted to higher frequencies relative to the correspondent ε'' peak, as theoretically predicted [46,47]. In addition, for the 40% preparation (Fig. 6b), a relaxational response superimposes the conductivity plot at intermediate and high frequencies.

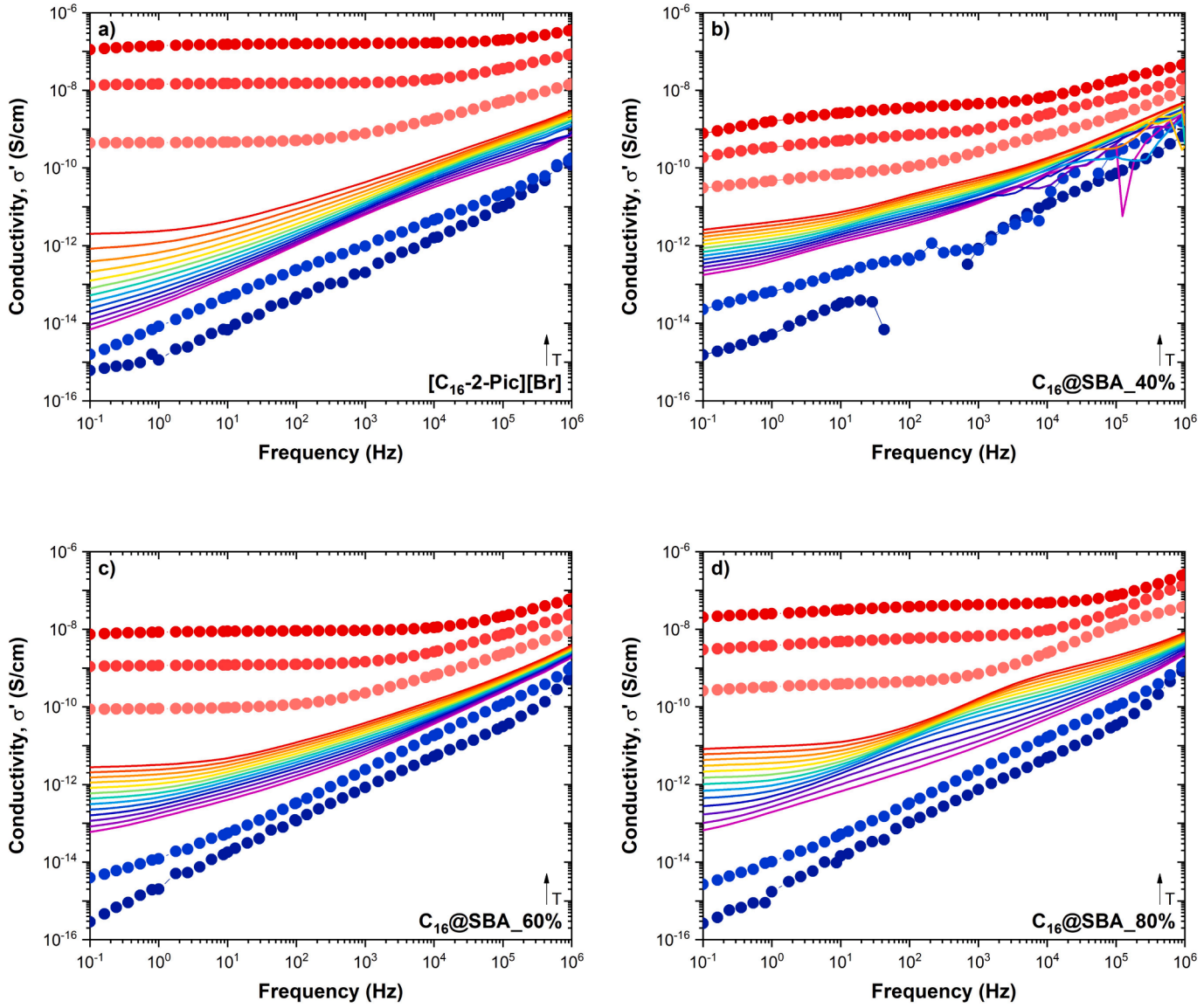

Fig. 5. Real conductivity spectra for a) [C_{16}-2-Pic][Br], b) C_{16}@SBA_40%, c) C_{16}@SBA_60% and d) C_{16}@SBA_80%. Blue circles correspond to the isotherms collected at –50 °C and –20 °C, solid lines to the ones obtained from 0 to 24 °C (every 2 °C) and red circles to the isotherms between 50 to 100 °C in steps of 25 °C.

3.3.2. *Modulus analysis*

To better disclose the underlying processes, spectra were analysed in the modulus representation. Fig. 7a to 7d display the isothermal spectra from –20 to 130 °C in steps of 10 °C. To guide the reader in order to compare the response of neat ILC and composites, the individual HN-type functions are included for spectra acquired at 20 °C. As it can be seen, the peaks of C_{16}, 40 and 60% preparations have an asymmetric shape, being simulated by a sum of two HN-type functions (Equation (2)). The existence of two underlying processes (purple and light red shadowed areas in Fig. 7a to 7d) is in line with the aforementioned existence of conductivity I and II contributions. For C_{16}@SBA_80%, it was necessary to consider an additional HN function (light blue shadowed area in Fig. 7d), which, from the comparison (Fig. 6c), was ascribed to a relaxational mode. Moreover, a low intense relaxation process (yellow shadowed area) was also considered for the hybrid materials in the high frequency side.

The extracted HN relaxation times, after transformation to a model independent τ_{max} through Equation (3), are plotted in Fig. 7e to 7h and compared with the σ_{dc} values estimated from Jonscher equation, which are included in the right axis as star-shaped symbols. Both left and right logarithmic scales have the same number of decades, turning clear the similarity between $\log(\sigma_{dc\_I})$ and $-\log(\tau_{max\_I})$ plots. This match between the *T*-dependence of the two properties confirms that the low-frequency M'' process is due to pure ohmic conductivity (conductivity I), supported also by the respective HN shape parameters: $\alpha_{HN} = \beta_{HN} = 1$. The contribution at intermediate frequencies (light red curve in Fig. 7e to 7h), that immediately follows the ohmic peak, is then associated, as previously stated, to a non-strictly ohmic contribution (conductivity II) assigned to the transition from *dc* to *ac* regime [89]. It is worthwhile noting how the deconvolution of the individual processes related with conductivity I and II is facilitated in the modulus formalism, which also allows to extract information until much lower temperatures when compared to the $\sigma'(f)$ analysis.

In Fig. 8, the different relaxation times are compared: a) conductivity I, b) conductivity II and c) relaxational processes. Regarding Fig. 8a, it is notorious the monotonic temperature dependence followed by $\tau_{M''}(1/T)$ in the composites, instead of the Arrhenian-like multiple regimes found for the neat ILC (diamonds). Therefore, upon incorporation in the nanoporous matrix, the ILC phase transition in 40 and 60% preparations was supressed, originating a VFTH (Equation (4)) temperature dependence of the relaxation times in the supercooled liquid state. This behaviour is typically found in glass forming materials [90], including

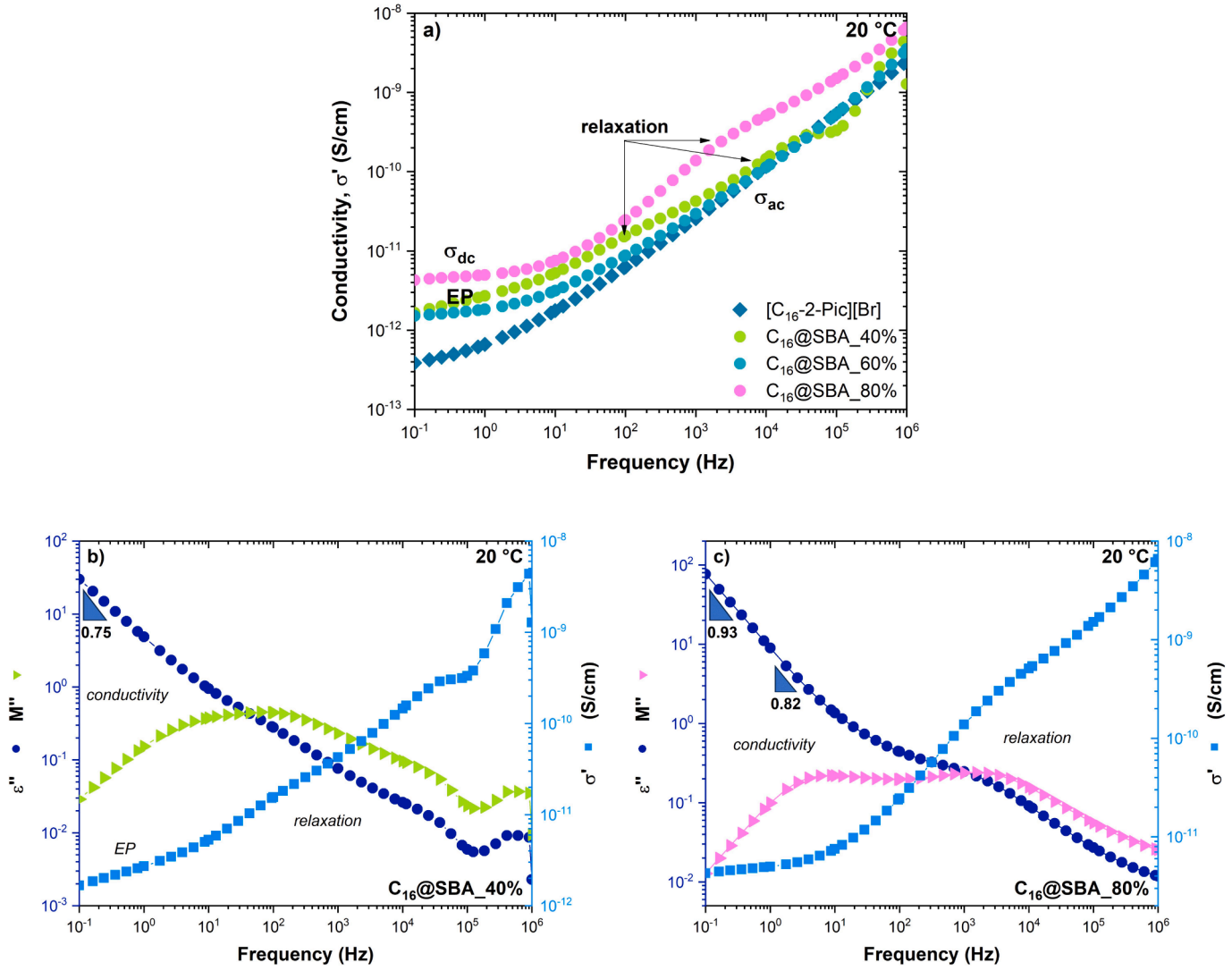

Fig. 6. a) Comparison between the real conductivity spectra at 20 °C for [C_{16}-2-Pic][Br] and the three composites, illustrating the different conductivity regimes, electrode polarisation and relaxation effects; dielectric response of b) C_{16}@SBA_40% and c) C_{16}@SBA_80% at the same temperature in σ′(*f*) (squares), M″(*f*) (triangles) and ε″(*f*) (circles) representations.

the lower member of the series [C_6-2-Pic][Br] [1]. The VFTH parameters are included in Table S1 under the designation of "modulus ohmic conductivity I", which also presents the corresponding parameters of the direct current conductivity. Although no clear evidence was provided by DRS of a glass transition relaxation process, the VFTH dependence of the relaxation times for charge migration can be taken as an indication of guest amorphisation. It is important to remember that vitrification was only detected by TMDSC at a higher temperature than the one estimated for neat ILC with a rather small discontinuity in the heat flow. These features are compatible with a highly hindered molecular mobility of the confined material, lacking of dielectric response associated with a glass transition. Indeed, for other ionic liquids incorporated in different nanostructured matrices, molecular dynamics simulations provided evidence low mobility of the guest close to the interface [91,92].

Although above 20 °C the relaxation rate is higher for the crystalline [C_{16}-2-Pic][Br], it is important to highlight that, below this temperature, the relaxation times for the process related to ohmic conductivity (shadowed area in Fig. 8a), conductivity I, are always shorter for the composites relative to neat C_{16}, indicating a faster charge migration inside pores. Also, the real conductivity at 0.1 Hz (Figure S5) evidences the better conductive behaviour of the hybrid materials between –20 and 20 °C, a range that covers the usual operating temperature window, representing another advantage of C_{16} incorporation in a porous matrix, despite the almost insulating character of the carrier. Regarding the process associated with conductivity II, it follows almost the same temperature dependence as the former. Nonetheless, data collapse into one chart at high temperatures for all systems, pointing to a similar origin (see Fig. 8b). For 40% composite, it exhibits the features of a relaxation process (remember Fig. 6a and 6c) that could be addressed to a sort of Maxwell-Wagner-Sillars [93,94] polarisation owing to either interfacial polarisation inside the supercooled/confined liquid material, arising from structural heterogeneities as ionic nanodomains [95], and/or, as expected in guest carrier systems [96], due to silica matrix/C_{16} interfaces. Therefore, conductivity II is the superposition of non-strictly ohmic conductivity associated with the *dc* to *ac* transition, as above mentioned, and interfacial polarisation.

Additionally, C_{16}@SBA_80% has a process with characteristics of a true dipolar relaxation located at intermediate frequencies. The respective isochronal ε″(T) plots, depicted in the inset of Fig. 8c, exhibit a mixed behaviour between a crystalline and a supercooled material. Indeed, at high frequencies, the Arrhenian *T*-dependence denotes a crystalline-like behaviour (delimited by the arrows), in line to what was observed for neat crystalline [C_{16}-2-Pic][Br] [1]. However, the frequency dependent peak in ε″(T) and the step in ε′(T) (Figure S6) are

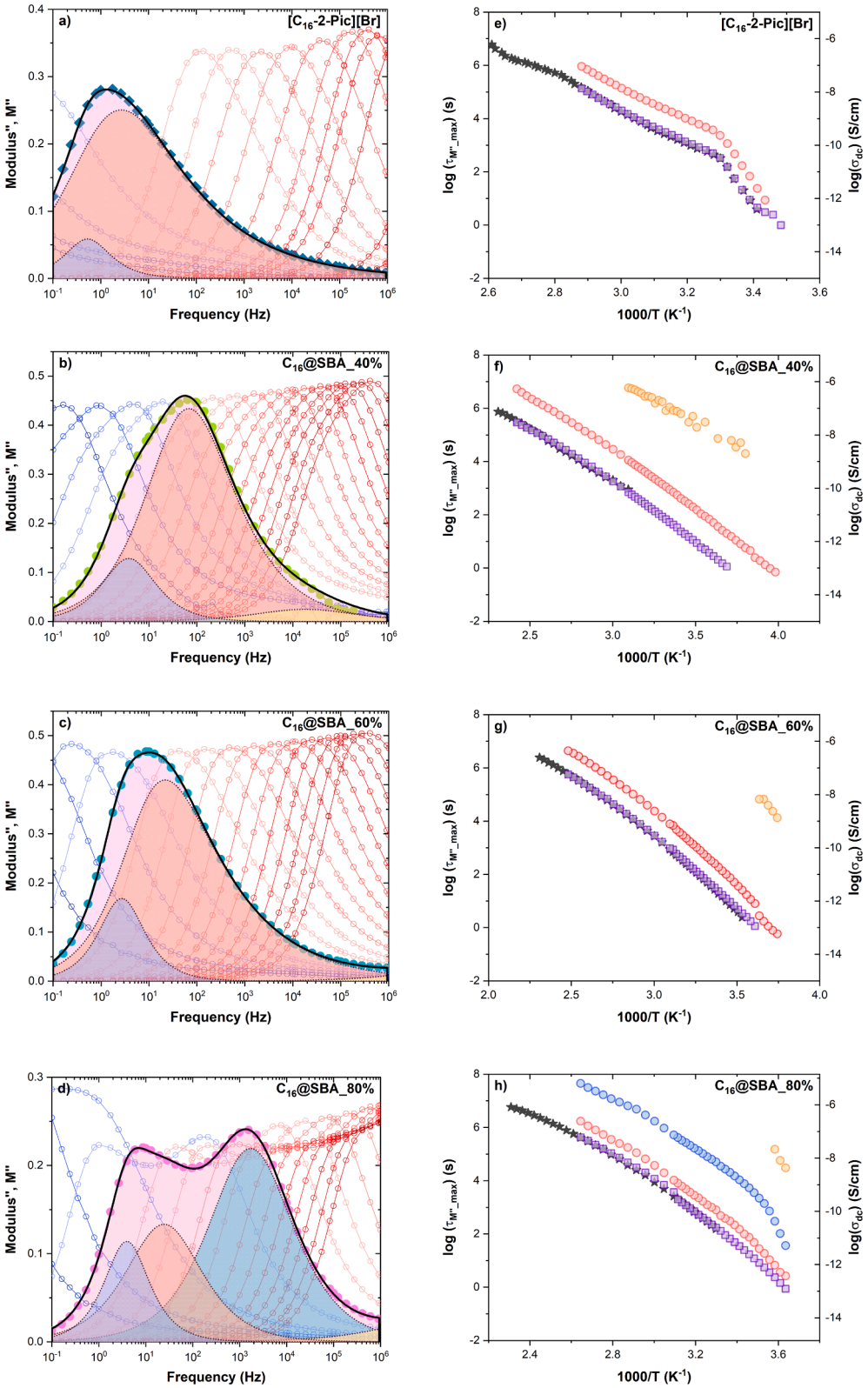

Fig. 7. Imaginary component of the complex electrical modulus for a) [C_{16}-2-Pic][Br], b) C_{16}@SBA_40% c) C_{16}@SBA_60% and d) C_{16}@SBA_80%. The isotherms are presented from –20 to 130 °C in steps of 10 °C, in which the spectrum collected at 20 °C is highlighted. The black solid line corresponds to the overall fit with a sum HN-type functions: conductivity I (purple), conductivity II (light red) and relaxation (light blue and yellow) processes. The respective relaxation times ($\tau_{M'}$) are plotted against the temperature reciprocal (different 1000/T scales were used), with the same colour scheme, and compared with σ_{dc} (star-shaped symbols) in Fig. 7e to 7h.

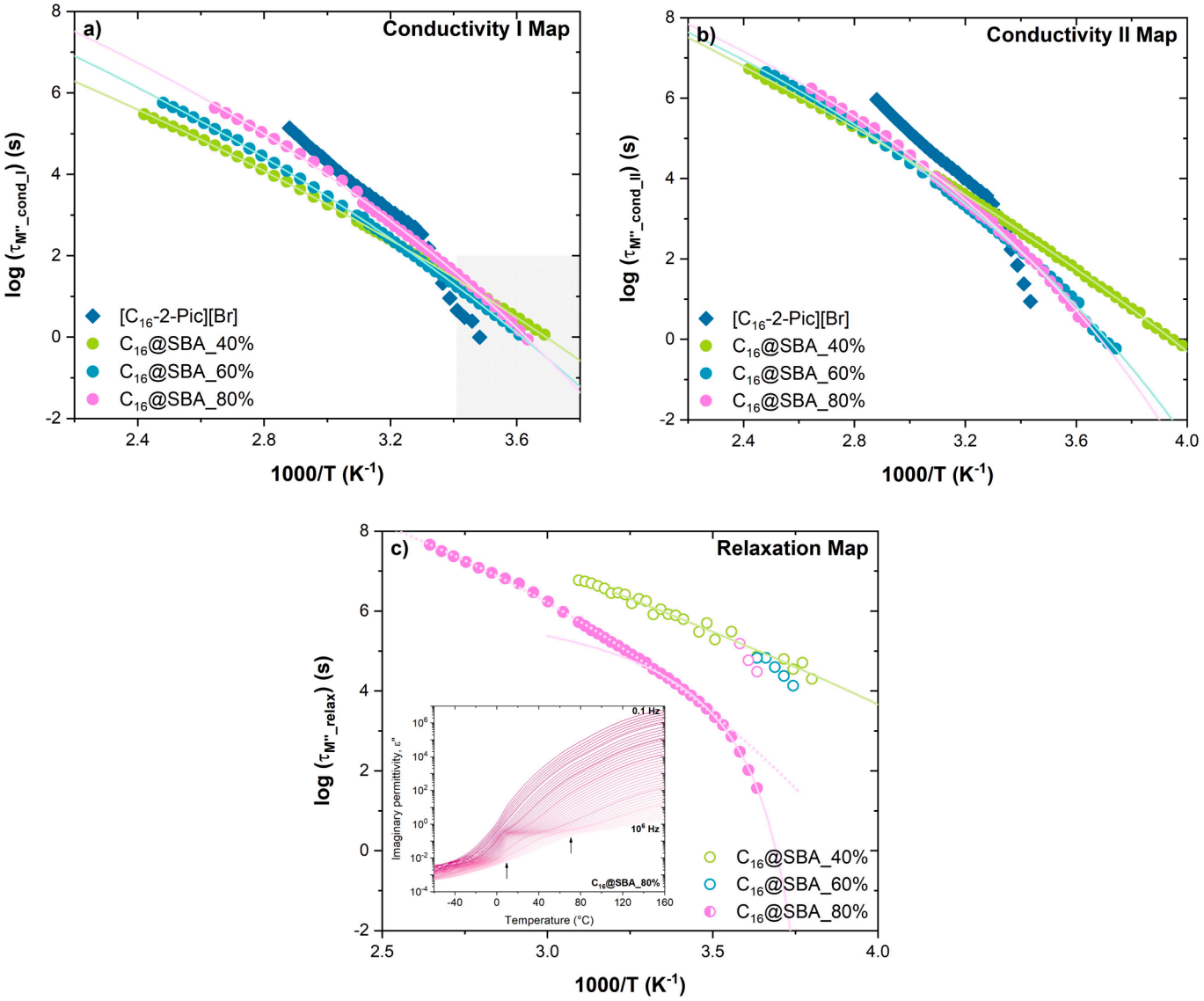

Fig. 8. Relaxation times extracted from the fit of the electrical modulus M″(*f*), through Equation (2), associated with: a) conductivity I, b) conductivity II and c) relaxational contributions. The inset of Fig. 8c represents the isochronal plot, ε″(T), for C_{16}@SBA_80%, whose arrows denote the crystalline-like behaviour in the high frequency range, whereas supercooled signature emerges at intermediate frequencies.

coherent with the relaxation process associated with a glass transition. Since this composite contains the greatest amount of ionic liquid, it is plausible to assume the coexistence of some uncrystallised confined liquid with a low-morph crystalline fraction within pores. The corresponding temperature dependence of the relaxation times requires more than one VFTH function to describe the overall data. Considering two VFTH laws, below and above 20 °C (pink solid and dotted lines in Fig. 8c, respectively), the one at lower temperatures can be extrapolated to τ = 100 s [97], taken as an empirical estimate of the glass transition temperature through dielectric measurements, yielding to $T_{g\_DRS\ (\tau=100s)}$ = –5.1 °C, a very close value to the previously estimated by the $2/3T_m$ rule (–8 °C). Therefore, in this temperature range, the probed dielectric response should be dominated by dipolar reorientation (ion pairs) in a supercooled-like state, as supported by the observation of: i) a frequency dependent behaviour in both ε′ and ε″(T) traces, denoting the kinetic nature of the glass transition phenomenon (inset of Fig. 8c), contrary to the purely thermodynamic melting event that should be *T*-invariant in the isochronal plot; ii) the obeyance of the extracted relaxation times to a VFTH law; and iii) the reasonable value for the glass transition temperature obtained by the extrapolation to τ = 100 s. This glass transition is not unequivocally detected by DSC, being probably submerged under the melting of the low-*T* morph. Another possibility is the conversion to a rotator crystalline phase. While an ideal crystal has a perfect crystalline order, plastic crystals possess some degree of internal disorder [98,99], as the ability of small molecular moieties to rotate or even vibrate with limited amplitude around the long molecular axis [100]. These so-called rotator phases occur in the range between the fully crystalline phase and the molten liquid [101], being reported for a variety of materials, including ionic liquids [101], methylimidazolium based ionic crystals [102] and *n*-alkanes [103,104]. Contrarily to a perfect crystal that lacks of dielectric response, materials exhibiting rotational degrees of freedom have a dielectric signature and temperature dependence of the respective relaxation times identical to a conventional glass former [105,106]. Therefore, it is hard to distinguish if the registered dielectric spectra are characteristic of a supercooled or a rotator phase. In fact, the latter hypothesis was already raised for [C_{16}-2-Pic][Br] [1], having an alkyl chain homologue to *n*-hexadecane for which a transient rotator phase was recently characterised [107]. This rotationally disordered phase in the neat ILC seems to emerge in the dielectric spectra between –20 and 16 °C (see arrow in Figure S7a).

Assuming that it persists under confinement, particularly for the 80% hybrid material, the dielectric strength of such rotationally disordered phase becomes highly enhanced, probably due to a higher amplitude of the respective dipolar fluctuations occurring in a less dense medium compared to bulk at the same temperature (Figure S7b).

Furthermore, the three composites present a high frequency relaxation (open circles in Fig. 8c), clearly detected on C_{16}@SBA_40%, which can be a relaxation process of [C_{16}-2-Pic][Br] when existing in such low density/high dispersed state. This fast relaxation could play a role in the charge transport of C_{16}@SBA_40%, as this preparation is the one exhibiting the highest conductivity at low temperatures.

3.3.3. *Impedance analysis*

An alternative way to compare the electrical performance of the prepared composites with neat ILC is through the complex impedance ($Z^*(\omega) = Z'(\omega) + jZ''(\omega)$), equivalent to the conductivity and modulus representations, as they are interrelated. When the symmetric of the imaginary part ($-Z''$) is represented against the real part (Z'), a so-called Nyquist plot is obtained. Such representation was performed for the herein studied systems at 20 °C and depicted in Fig. 9. Contrary to the conductivity and modulus analyses, in which the frequency is explicit, in the Nyquist plot, the frequency is hidden in the high frequency region, being plotted towards the origin (left side) and the low frequency region outward from the x,y origin (right side) [108].

When an ideal Voigt circuit [109] is considered, a relaxation element, $R/(1 + j\omega\tau)$, is assumed, consisting of a parallel combination of a resistor (R) and a capacitor (C), in which the relaxation time (τ) is equal to the product R × C; R corresponds to the semi-circle diameter and τ to the frequency reciprocal of Z'' maximum. For such Voigt circuit element, the $-Z''$ *vs.* Z' representation gives rise to a perfect semi-circle [110–113]. This was not strictly observed for the hybrid materials nor neat ILC [1]. Instead, skewed or depressed arcs in the complex plane are obtained. In general, the non-ideal behaviour is caused by inhomogeneity of charge carriers' distribution caused by structure heterogeneities, such as grain boundaries, crystal defects [114] or even guest–host interfaces, leading to distributed relaxations with different time constants. The modulus analysis already revealed the need to assume processes with a distribution of relaxation times (α and $\beta \neq 1$) to adequately simulate the spectra. The α parameter assumed in the equations describing the equivalent circuits of neat ILC and composites $R/(1+(j\omega\tau)^{\alpha})$ is a measure of such distribution of relaxation times: $\alpha = 1$, for Debye elements and < 1 for real circuits (see the respective values in Figure S8). Concerning C_{16}@SBA_40%, an inclined spike [106] is observed in the Nyquist plot due to electrode polarisation. This effect negatively impacts the conductivity that decreases at the lowest frequencies owing to the extra capacitance arising from blocked charges. The plot at a higher temperature (40 °C), displayed in the inset of Fig. 9, confirms the attribution to electrode polarisation since this effect increases with the temperature increasing. Therefore, electrode polarisation was taken into account by adding a parallel combination of a resistor and a constant phase element (CPE) [115] to the bulk equivalent electrical circuit (Figure S8). Moreover, for C_{16}@SBA_40%, CPE admittance and intrinsic capacitance increase from 20 °C ($Y_0 = 48$; C = 91 nF) to 40 °C ($Y_0 = 7080$; C = 7250 nF) due to the rise of blocked charges at the origin of EP effect. Such electrode polarisation contribution was also considered in the simulation of 80% preparation, although at much lower level. In fact, at 20 °C, the associated capacitance in C_{16}@SBA_80% is tenfold lower relative to the 40%. For neat C_{16} and 60% composite, no EP was detected at this temperature. The solid lines in the Nyquist plots (Fig. 9) represent the fit to the experimental data, resulting from the simultaneous analysis of six different properties (C', C'', M', M'', Z' and Z'' (f), Figure S9) instead of just Z' and Z'', which is not as sensitive to the processes occurring at moderate and high frequencies. The fittings quality also validates the proposed equivalent circuits.

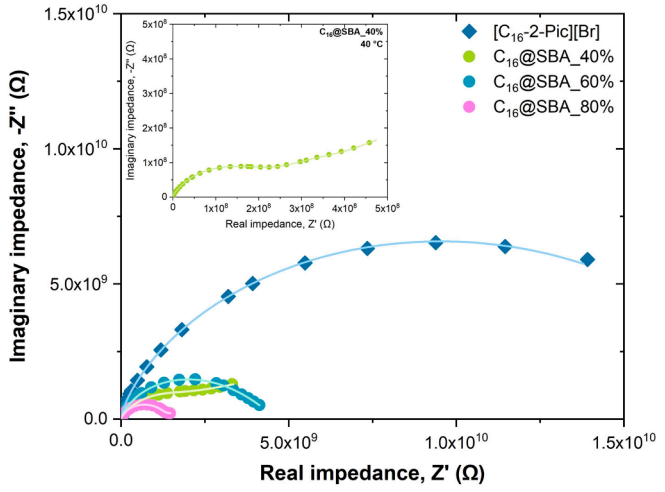

Fig. 9. Nyquist plots at 20 °C for [C_{16}-2-Pic][Br] and the three composites. Impedances measured at high frequencies lie on the right side and those measured at low frequencies on the left. The solid lines are the theoretical simulation through the equivalent circuits proposed in Figure S8. The inset is the Nyquist representation for C_{16}@SBA_40% at 40 °C, in which the spike due to electrode polarisation is enhanced.

It is important to mention that the conductivity isotherm of C_{16}@SBA_40% at lower temperatures, e.g., –10 °C (Figure S10), seems to exhibit a sort of crossover frequency. However, the decrease is not caused by EP, as the correspondent Nyquist plot does not show a spike. Instead, the arc is starting to be defined, suggesting the impossibility of building a continuous percolation path to enable *dc*- conductivity due to insufficient loading that gives rise to interrupted charge migration pathway.

Additionally, the radii of the arcs obtained for the most loaded hybrid materials, 60 and 80%, are the shortest, meaning that both resistance and relaxation time of charge migration are inferior [116] relative to C_{16}. Therefore, the incorporation in the silica matrix allowed a faster charge migration, due to a modification of the guest physical state, converting to more mobile arrangements. Furthermore, the insignificant effect of electrode polarisation, especially in the case of the 60% preparation, and contrary to what was observed for the homologous [C_6-2-Pic][Br] glass former [1], which is highly affected by electrode polarisation, indicates that charge transport and discharge at the electrodes might be mediated by the silica host. Therefore, it was possible, through nanoconfinement, to take advantage of the amorphous state, improving conductivity without the inconvenience of high EP.

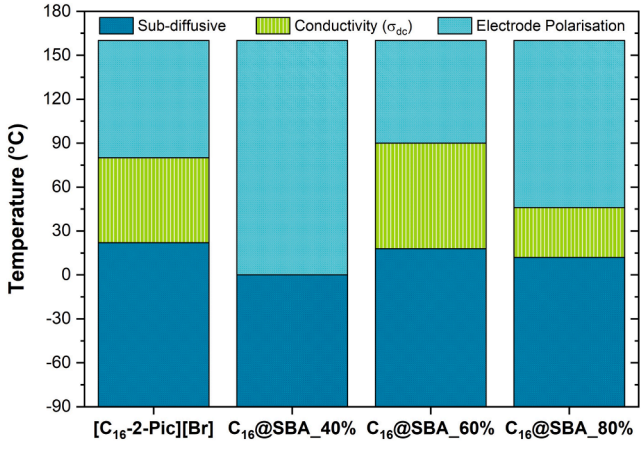

Fig. 10. Schematic comparison of the conductivity behaviour for [C_{16}-2-Pic][Br] and the composites, emphasising the regions where electrode polarisation, *dc*- and *ac*-conductivity are observed.

The overview of the conductivity behaviour found for all materials is summarised in Fig. 10, highlighting the potential of these silica incorporated composites. In the region where 60 and 80% preparations exhibit pure σ_{dc}, the conductivity is around one decade higher than the one of neat C_{16}. Moreover, the window where direct current conductivity emerges is wider for C_{16}@SBA_60%, which is also the material least affected by electrode polarisation, even when compared to [C_{16}-2-Pic][Br]. These characteristics, along with its long-term stability, point out the 60% composite as the one presenting the best performance in –20 to 20 °C.

4. Conclusions

This work reports the investigation of hybrid materials produced by confining the ionic liquid crystal [C_{16}-2-Pic][Br] in mesoporous SBA-15 silica (6.8 nm) in three different weight ratios: 40, 60 and 80% w/w. While the neat ILC undergoes several crystal-crystal transitions and a smectic A mesophase, these are suppressed in the least loaded composites (40 and 60%), which only exhibit a glass transition around 20 °C. The low intensity of the respective heat capacity step and significantly higher glass transition temperature value seem to support that the material is in a hindered dynamic state, lacking of a correspondent dielectric response. This amorphous/supercooled state remains stable for more than one year, which is a plus over the neat ILC undergoing polymorphic conversion that depends on the thermal history. In the 80% preparation, the material crystallises intra-pores in a low-*T* morph. Nevertheless, the respective dielectric behaviour shows the features of a true relaxation process, pointing to the coexistence of a bulk-like amorphous/supercooled phase ($T_g \sim -5$ °C) or a highly mobile rotor phase with a crystalline low-*T* morph fraction.

Aiming the use in electronic devices, the conductive behaviour of the prepared hybrid materials was evaluated. For C_{16}@SBA_40%, *dc*-conductivity is never attained due electrode polarisation and, probably, insufficient loading that impairs continuous charge transport pathways. However, its high dispersion in the silica matrix allowed to better disclose a high frequency process that could play a role in charge transport at cryogenic temperatures. Notably, and despite the almost insulating nature of SBA-15 matrix, all composites revealed, through impedance analysis and corresponding Nyquist plots, lower resistance and faster charge migration compared to the neat ILC between –20 and 20 °C, which includes the usual operating temperature window. From a fundamental point of view, this work highlights the importance of electrical modulus analysis, as it allows to characterise the studied materials not only until a much lower temperature, but also to deconvolute overall conductivity in multiple processes.

Under a practical perspective, the introduction of some degree of disorder positively impacts the conductivity in that *T*-range, which could also involve a silica assisted pathway. Moreover, the relaxation times of conductivity I and II, extracted from the electrical modulus analysis, revealed to follow a single VFTH law in all composites. This makes their conductive behaviour more predictable relative to [C_{16}-2-Pic][Br], exhibiting multiple Arrhenian branches. Furthermore, the conversion to an amorphous/supercooled material with the corresponding conductivity improvement was achieved without significant manifestation of undesirable EP effect and so the silica carrier seems to play a role also in discharging at the electrodes. This was particularly relevant for C_{16}@SBA_60%, showing the best compromise between bulk conductivity, phase stability inside pores and lack of electrode polarisation between –20 to 20 °C. Finally, the low price of the silica matrix allows to obtain cost-efficient solid electronic devices with liquid-like conductive features that outperform the neat ionic liquid crystal at ambient temperature.

CRediT authorship contribution statement

Andreia F.M. Santos: Writing – review & editing, Writing – original draft, Visualization, Methodology, Investigation. **M. Teresa Viciosa:** Writing – review & editing, Validation, Software, Formal analysis, Data curation. **Inês Matos:** Methodology, Investigation. **João C. Sotomayor:** Methodology, Investigation. **João L. Figueirinhas:** Writing – review & editing, Methodology, Investigation, Formal analysis. **Maria H. Godinho:** Writing – review & editing, Methodology, Formal analysis. **Luis C. Branco:** Writing – review & editing, Resources, Project administration, Conceptualization. **C.J. Dias:** Writing – review & editing, Writing – original draft, Software, Formal analysis, Data curation, Conceptualization. **Madalena Dionísio:** Writing – review & editing, Writing – original draft, Supervision, Formal analysis, Conceptualization.

Declaration of competing interest

The authors declare that they have no known competing financial interests or personal relationships that could have appeared to influence the work reported in this paper.

Data availability

Data will be made available on request.

Acknowledgments

This work was supported by the Associate Laboratory for Green Chemistry LAQV, Portugal, (LA/P/0008/2020, UIDB/50006/2020, UIDP/50006/2020), i3N, Portugal, (LA/P/0037/2020, UIDB/50025/2020, UIDP/50025/2020), CQE, Portugal, (UIDB/00100/2020, UIDP/00100/2020) and CeFEMA, Portugal, (UIDB/04540/2020, UIDP/04540/2020), which are financed by national funds from FCT-MCTES, Portugal, and by FEDER funds through the COMPETE 2020, Portugal, Program. The authors also thank the National Funds through FCT-MCTES, Portugal and POR Lisboa 2020, under the project numbers PTDC/EAM-AMB/2023/2021 (SUSTECH4H2O), POCI-01-0145-FEDER-007688 and European Interdisciplinary Action (COST Action, Belgium, CA21159, PhoBioS). A. F. M. Santos also acknowledges FCT-MCTES, Portugal, for the PhD Grant (SFRH/BD/132551/2017) and I. Matos for the contract CEECIND/004431/2022.

Appendix A. Supplementary data

Supplementary data to this article can be found online at https://doi.org/10.1016/j.molliq.2024.124830.

References

[1] A.F.M. Santos, J.L. Figueirinhas, C.J. Dias, M.H. Godinho, L.C. Branco, M. Dionísio, Study of the mesomorphic properties and conductivity of *n*-alkyl-2-picolinium ionic liquid crystals, J. Mol. Liq. 377 (2023) 121456, https://doi.org/10.1016/j.molliq.2023.121456.

[2] O. Werzer, N. Boucher, J.P. de Silva, G. Gbabode, Y.H. Geerts, O. Konovalov, A. Moser, J. Novak, R. Resel, M. Sferrazza, Interface Induced Crystal Structures of Dioctyl-Terthiophene Thin Films, Langmuir. 28 (2012) 8530–8536, https://doi.org/10.1021/la301213d.

[3] Y. Fu, T. Wu, J. Wang, J. Zhai, M.J. Shearer, Y. Zhao, R.J. Hamers, E. Kan, K. Deng, X.-Y. Zhu, S. Jin, Stabilization of the Metastable Lead Iodide Perovskite Phase via Surface Functionalization, Nano Lett. 17 (2017) 4405–4414, https://doi.org/10.1021/acs.nanolett.7b01500.

[4] H.M.A. Ehmann, O. Werzer, Surface Mediated Structures: Stabilization of Metastable Polymorphs on the Example of Paracetamol, Cryst. Growth Des. 14 (2014) 3680–3684, https://doi.org/10.1021/cg500573e.

[5] Y. Zhou, J. Kwun, H.F. Garces, S. Pang, N.P. Padture, Observation of phase-retention behavior of the $HC(NH_2)_2PbI_3$ black perovskite polymorph upon mesoporous TiO_2 scaffolds, Chem. Commun. 52 (2016) 7273–7275, https://doi.org/10.1039/c6cc02086k.

[6] D. Reischl, C. Röthel, P. Christian, E. Roblegg, H.M.A. Ehmann, I. Salzmann, O. Werzer, Surface-Induced Polymorphism as a Tool for Enhanced Dissolution: The Example of Phenytoin, Cryst. Growth Des. 15 (2015) 4687–4693, https://doi.org/10.1021/acs.cgd.5b01002.

[7] Y. Cao, K. Zhang, Z. Gao, J. Wang, S. Rohani, J. Gong, Preparation, Stabilization, and Dissolution Enhancement of Vortioxetine Hydrobromide Metastable

Polymorphs in Silica Nanopores, Cryst. Growth Des. 22 (2022) 191–199, https://doi.org/10.1021/acs.cgd.1c00825.
[8] F. Kremer, Dynamics in Geometrical Confinement, Springer (2014), https://doi.org/10.1007/978-3-319-06100-9.
[9] K. Minami, F. Mizuno, A. Hayashi, M. Tatsumisago, Lithium ion conductivity of the Li_2S-P_2S_5 glass-based electrolytes prepared by the melt quenching method, Solid State Ion. 178 (2007) 837–841, https://doi.org/10.1016/j.ssi.2007.03.001.
[10] D. Wohlmuth, V. Epp, P. Bottke, I. Hanzu, B. Bitschnau, I. Letofsky-Papst, M. Kriechbaum, H. Amenitsch, F. Hofer, M. Wilkening, Order *vs.* disorder—a huge increase in ionic conductivity of nanocrystalline $LiAlO_2$ embedded in an amorphous-like matrix of lithium aluminate, J. Mater. Chem. A 2 (2014) 20295–20306, https://doi.org/10.1039/c4ta02923b.
[11] J.A. Dawson, M.S. Islam, A Nanoscale Design Approach for Enhancing the Li-Ion Conductivity of the $Li_{10}GeP_2S_{12}$Solid Electrolyte, ACS Mater. Lett. 4 (2022) 424–431, https://doi.org/10.1021/acsmaterialslett.1c00766.
[12] P. Heitjans, M. Masoud, A. Feldhoff, M. Wilkening, NMR and impedance studies of nanocrystalline and amorphous ion conductors: lithium niobate as a model system, Faraday Discuss. 134 (2007) 67–82, https://doi.org/10.1039/b602887j.
[13] C. Li, L. Gu, J. Maier, Enhancement of the Li Conductivity in LiF by Introducing Glass/Crystal Interfaces, Adv. Funct. Mater. 22 (2012) 1145–1149, https://doi.org/10.1002/adfm.201101798.
[14] E. Hüger, L. Dörrer, J. Rahn, T. Panzner, J. Stahn, G. Lilienkamp, H. Schmidt, Lithium Transport through Nanosized Amorphous Silicon Layers, Nano Lett. 13 (2013) 1237–1244, https://doi.org/10.1021/nl304736t.
[15] L. Schweiger, K. Hogrefe, B. Gadermaier, J.L.M. Rupp, H.M.R. Wilkening, Ionic Conductivity of Nanocrystalline and Amorphous $Li_{10}GeP_2S_{12}$: The Detrimental Impact of Local Disorder on Ion Transport, J. Am. Chem. Soc. 144 (2022) 9597–9609, https://doi.org/10.1021/jacs.1c13477.
[16] B. Gadermaier, L. Resch, D.M. Pickup, I. Hanghofer, I. Hanzu, P. Heitjans, W. Sprengel, R. Würschum, A.V. Chadwick, H.M.R. Wilkening, Influence of defects on ionic transport in $LiTaO_3$ – A study using EXAFS and positron annihilation lifetime spectroscopy, Solid State Ion. 352 (2020) 115355, https://doi.org/10.1016/j.ssi.2020.115355.
[17] J. Maier, Nanoionics: ion transport and electrochemical storage in confined systems, Nat. Mater. 4 (2005) 805–815, https://doi.org/10.1038/nmat1513.
[18] A. Hayashi, K. Noi, A. Sakuda, M. Tatsumisago, Superionic glass-ceramic electrolytes for room-temperature rechargeable sodium batteries, Nat. Commun. 3 (2012) 856, https://doi.org/10.1038/ncomms1843.
[19] M. Wilkening, V. Epp, A. Feldhoff, P. Heitjans, Tuning the Li diffusivity of poor ionic conductors by mechanical treatment: High Li conductivity of strongly defective $LiTaO_3$ nanoparticles, J. Phys. Chem. C 112 (2008) 9291–9300, https://doi.org/10.1021/jp801537s.
[20] M. Beiner, G.T. Rengarajan, S. Pankaj, D. Enke, M. Steinhart, Manipulating the Crystalline State of Pharmaceuticals by Nanoconfinement, Nano Lett. 7 (2007) 1381–1385, https://doi.org/10.1021/nl0705081.
[21] D. Zhao, J. Feng, Q. Huo, N. Melosh, G.H. Fredrickson, B.F. Chmelka, G.D. Stucky, Triblock Copolymer Syntheses of Mesoporous Silica with Periodic 50 to 300 Angstrom Pores, Science. 279 (1998) 548–552, https://doi.org/10.1126/science.279.5350.548.
[22] Z.A. ALOthman, A Review, Fundamental Aspects of Silicate Mesoporous Materials, Materials. 5 (2012) 2874–2902, https://doi.org/10.3390/ma5122874.
[23] M. Shakeri, Z.K. Shal, P. Van Der Voort, An Overview of the Challenges and Progress of Synthesis, Characterization and Applications of Plugged SBA-15 Materials for Heterogeneous Catalysis, Materials. 14 (2021) 5082, https://doi.org/10.3390/ma14175082.
[24] O.A. Anunziata, M.L. Martínez, A.R. Beltramone, Hydroxyapatite/MCM-41 and SBA-15 Nano-composites: Preparation, Characterization and Applications, Materials. 2 (2009) 1508–1519, https://doi.org/10.3390/ma2041508.
[25] S. Yuan, M. Wang, J. Liu, B. Guo, Recent advances of SBA-15-based composites as the heterogeneous catalysts in water decontamination: A mini-review, J. Environ. Manage. 254 (2020) 109787, https://doi.org/10.1016/j.jenvman.2019.109787.
[26] S. Shin, H.S. Kim, M. Il Kim, J. Lee, H.G. Park, J. Kim, Crowding and confinement effects on enzyme stability in mesoporous silicas, Int. J. Biol. Macromol. 144 (2020) 118–126, https://doi.org/10.1016/j.ijbiomac.2019.12.034.
[27] Y. Wang, Q. Zhao, N. Han, L. Bai, J. Li, J. Liu, E. Che, L. Hu, Q. Zhang, T. Jiang, S. Wang, Mesoporous silica nanoparticles in drug delivery and biomedical applications, Nanomedicine, NBM. 11 (2015) 313–327, https://doi.org/10.1016/j.nano.2014.09.014.
[28] D.M. Galindres, D. Cifuentes, L.E. Tinoco, Y. Murillo-Acevedo, M.M. Rodrigo, A.C. F. Ribeiro, M.A. Esteso, A Review of the Application of Resorcinarenes and SBA-15 in Drug Delivery, Processes. 10 (2022) 684, https://doi.org/10.3390/pr10040684.
[29] P. Kolimi, S. Narala, A.A.A. Youssef, D. Nyavanandi, N. Dudhipala, A systemic review on development of mesoporous nanoparticles as a vehicle for transdermal drug delivery, Nanotheranostics. 7 (2023) 70–89, https://doi.org/10.7150/ntno.77395.
[30] Ł. Laskowski, M. Laskowska, N. Vila, M. Schabikowski, A. Walcarius, Mesoporous Silica-Based Materials for Electronics-Oriented Applications, Molecules. 24 (2019) 2395, https://doi.org/10.3390/molecules24132395.
[31] J. Otomo, S. Wang, H. Takahashi, H. Nagamoto, Microstructure development of mesoporous silica thin films with pore channels aligned perpendicularly to electrode surfaces and application to proton conducting composite electrolyte membranes, J. Memb. Sci. 279 (2006) 256–265, https://doi.org/10.1016/j.memsci.2005.12.013.
[32] P.A.R.D. Jayathilaka, M.A.K.L. Dissanayake, I. Albinsson, B.-E. Mellander, Effect of nano-porous Al_2O_3 on thermal, dielectric and transport properties of the (PEO)$_9$LiTFSI polymer electrolyte system, Electrochim. Acta. 47 (2002) 3257–3268, https://doi.org/10.1016/S0013-4686(02)00243-8.
[33] W. Li, J. Liu, D. Zhao, Mesoporous materials for energy conversion and storage devices, Nat. Rev. Mater. 1 (2016) 16023, https://doi.org/10.1038/natrevmats.2016.23.
[34] Y.-K. Sun, Promising All-Solid-State Batteries for Future Electric Vehicles, ACS Energy Lett. 5 (2020) 3221–3223, https://doi.org/10.1021/acsenergylett.0c01977.
[35] Z. Rajabi, M. Javanbakht, K. Hooshyari, A. Badiei, M. Adibi, High temperature composite membranes based on polybenzimidazole and dendrimer amine functionalized SBA-15 mesoporous silica for fuel cells, New J. Chem. 44 (2020) 5001–5018, https://doi.org/10.1039/c9nj05369g.
[36] B. Paul, A. Mahmud-Ali, M. Lenninger, S. Eberle, I. Bernt, D. Mayer, T. Bechtold, Silica incorporated cellulose fibres as green concept for textiles with reduced flammability, Polym. Degrad. Stab. 195 (2022) 109808, https://doi.org/10.1016/j.polymdegradstab.2021.109808.
[37] N. Abdou, B. Alonso, N. Brun, P. Landois, A. Taubert, P. Hesemann, A. Mehdi, Ionic guest in ionic host: ionosilica ionogel composites *via* ionic liquid confinement in ionosilica supports, Mater. Chem. Front. 6 (2022) 939–947, https://doi.org/10.1039/D2QM00021K.
[38] C. Yu, S. Ganapathy, E.R.H. Van Eck, H. Wang, S. Basak, Z. Li, M. Wagemaker, Accessing the bottleneck in all-solid state batteries, lithium-ion transport over the solid-electrolyte-electrode interface, Nat. Commun. 8 (2017) 1086, https://doi.org/10.1038/s41467-017-01187-y.
[39] L. Gao, Y. Wang, J. Wang, L. Huang, L. Shi, X. Fan, Z. Zou, T. Yu, M. Zhu, Z. Li, A Novel ZnII-Sensitive Fluorescent Chemosensor Assembled within Aminopropyl-Functionalized Mesoporous SBA-15, Inorg. Chem. 45 (2006) 6844–6850, https://doi.org/10.1021/ic0516562.
[40] W. Beichel, P. Eiden, I. Krossing, Establishing Consistent van der Waals Volumes of Polyatomic Ions from Crystal Structures, ChemPhysChem. 14 (2013) 3221–3226, https://doi.org/10.1002/cphc.201300659.
[41] N.G. McCrum, B.E. Read, G. Williams, Anelastic and Dielectric Effects in Polymeric Solids, Dover Publications, 1991.
[42] C.J. Dias, A Kramers-Kronig integral relation turned into a simple convolution operation and its application to dielectric measurements, Appl. Phys. Lett. 103 (2013) 222903, https://doi.org/10.1063/1.4834315.
[43] H. Matsuura, R. Shirakashi, Exclusion of DC conductivity effect from dielectric loss spectrum using Kramers-Kronig relations for evaluation of slow dynamics of water molecules, Jpn. J. Appl. Phys. 61 (2022) 068003, https://doi.org/10.35848/1347-4065/ac6afe.
[44] S. Havriliak, S. Negami, A complex plane analysis of α-dispersions in some polymer systems, J. Polym. Sci. C Polym. Symp. 14 (1966) 99–117, https://doi.org/10.1002/polc.5070140111.
[45] S. Havriliak, S. Negami, A complex plane representation of dielectric and mechanical relaxation processes in some polymers, Polymer. 8 (1967) 161–210, https://doi.org/10.1016/0032-3861(67)90021-3.
[46] F. Kremer, A. Schönhals, Broadband Dielectric Spectroscopy, Springer, Berlin (2003), https://doi.org/10.1007/978-3-642-56120-7.
[47] M. Wübbenhorst, J. van Turnhout, Analysis of complex dielectric spectra. I. One-dimensional derivative techniques and three-dimensional modelling, J. Non-Cryst. Solids. 305 (2002) 40–49, https://doi.org/10.1016/S0022-3093(02)01086-4.
[48] A.K. Jonscher, The "universal" dielectric response, Nature. 267 (1977) 673–679, https://doi.org/10.1038/267673a0.
[49] Y. Ohki, Broadband Complex Permittivity and Electric Modulus Spectra for Dielectric Materials Research, IEEJ Trans. Electr. Electron. Eng. 17 (2022) 958–972, https://doi.org/10.1002/tee.23565.
[50] H. Vogel, Das Temperaturabhangigkeitsgesetz der Viskositat von Flussigkeiten, Phys. Zeitschrift. 22 (1921) 645–646.
[51] G.S. Fulcher, Analysis of Recent Measurements of the Viscosity of Glasses, J. Am. Ceram. Soc. 8 (1925) 339–355, https://doi.org/10.1111/j.1151-2916.1925.tb16731.x.
[52] G. Tammann, W. Hesse, Die Abhängigkeit der Viscosität von der Temperatur bie unterkühlten Flüssigkeiten, Zeitschrift Für Anorg. Und Allg, Chemie. 156 (1926) 245–257, https://doi.org/10.1002/zaac.19261560121.
[53] M. Thommes, K. Kaneko, A.V. Neimark, J.P. Olivier, F. Rodriguez-Reinoso, J. Rouquerol, K.S.W. Sing, Physisorption of gases, with special reference to the evaluation of surface area and pore size distribution (IUPAC Technical Report), Pure Appl. Chem. 87 (2015) 1051–1069, https://doi.org/10.1515/pac-2014-1117.
[54] K.S.W. Sing, R.T. Williams, Physisorption Hysteresis Loops and the Characterization of Nanoporous Materials, Adsorpt. Sci. Technol. 22 (2004) 773–782, https://doi.org/10.1260/0263617053499032.
[55] I. Izquierdo-Barba, Á. Martinez, A.L. Doadrio, J. Pérez-Pariente, M. Vallet-Regí, Release evaluation of drugs from ordered three-dimensional silica structures, Eur. J. Pharm. Sci. 26 (2005) 365–373, https://doi.org/10.1016/j.ejps.2005.06.009.
[56] R.J. Ahern, J.P. Hanrahan, J.M. Tobin, K.B. Ryan, A.M. Crean, Comparison of fenofibrate–mesoporous silica drug-loading processes for enhanced drug delivery, Eur. J. Pharm. Sci. 50 (2013) 400–409, https://doi.org/10.1016/j.ejps.2013.08.026.
[57] T. Azaïs, C. Tourné-Péteilh, F. Aussenac, N. Baccile, C. Coelho, J.-M. Devoisselle, F. Babonneau, Solid-State NMR Study of Ibuprofen Confined in MCM-41 Material, Chem. Mater. 18 (2006) 6382–6390, https://doi.org/10.1021/cm061551c.
[58] Y.-J. Cheng, A.-Q. Zhang, J.-J. Hu, F. He, X. Zeng, X.-Z. Zhang, Multifunctional Peptide-Amphiphile End-Capped Mesoporous Silica Nanoparticles for Tumor

Targeting Drug Delivery, ACS Appl. Mater. Interfaces. 9 (2017) 2093–2103, https://doi.org/10.1021/acsami.6b12647.
[59] T. Cordeiro, I. Matos, F. Danède, J.C. Sotomayor, I.M. Fonseca, M.C. Corvo, M. Dionísio, M.T. Viciosa, F. Affouard, N.T. Correia, Evidence of Strong Guest-Host Interactions in Simvastatin Loaded in Mesoporous Silica MCM-41, Pharmaceutics. 15 (2023) 1320, https://doi.org/10.3390/pharmaceutics15051320.
[60] G. Calzaferri, S.H. Gallagher, D. Brühwiler, Multiple equilibria describe the complete adsorption isotherms of nonporous, microporous, and mesoporous adsorbents, Microporous Mesoporous Mater. 330 (2022) 111563, https://doi.org/10.1016/j.micromeso.2021.111563.
[61] M. Barczak, M. Gil, K. Terpiłowski, D. Kamiński, P. Borowski, Influence of bridged monomer on porosity and sorption properties of mesoporous silicas functionalized with diethylenetriamine groups, Adsorption. 25 (2019) 575–589, https://doi.org/10.1007/s10450-019-00047-z.
[62] M. Barczak, Amine-modified mesoporous silicas: Morphology-controlled synthesis toward efficient removal of pharmaceuticals, Microporous Mesoporous Mater. 278 (2019) 354–365, https://doi.org/10.1016/j.micromeso.2019.01.012.
[63] P. d'Orey, T. Cordeiro, M.A.O. Lourenço, I. Matos, F. Danède, J.C. Sotomayor, I. M. Fonseca, P. Ferreira, N.T. Correia, M. Dionísio, How Molecular Mobility, Physical State, and Drug Distribution Influence the Naproxen Release Profile from Different Mesoporous Silica Matrices, Mol. Pharm. 18 (2021) 898–914, https://doi.org/10.1021/acs.molpharmaceut.0c00908.
[64] H. Yu, Q.-Z. Zhai, Mesoporous SBA-15 molecular sieve as a carrier for controlled release of nimodipine, Microporous Mesoporous Mater. 123 (2009) 298–305, https://doi.org/10.1016/j.micromeso.2009.04.013.
[65] M.E. Adrover, M. Pedernera, M. Bonne, B. Lebeau, V. Bucalá, L. Gallo, Synthesis and characterization of mesoporous SBA-15 and SBA-16 as carriers to improve albendazole dissolution rate, Saudi Pharm. J. 28 (2020) 15–24, https://doi.org/10.1016/j.jsps.2019.11.002.
[66] Q.N. Khanh Nguyen, N.T. Yen, N.D. Hau, H.L. Tran, Synthesis and Characterization of Mesoporous Silica SBA-15 and ZnO/SBA-15 Photocatalytic Materials from the Ash of Brickyards, J. Chem. (2020 (2020)) 8456194, https://doi.org/10.1155/2020/8456194.
[67] M. Alcoutlabi, G.B. McKenna, Effects of confinement on material behaviour at the nanometre size scale, J. Phys. Condens. Matter. 17 (2005) R461, https://doi.org/10.1088/0953-8984/17/15/R01.
[68] R. Berwanger, A. Henschel, K. Knorr, P. Huber, R. Pelster, Phase transitions and molecular dynamics of n-hexadecanol confined in silicon nanochannels, Phys. Rev. B 79 (2009) 125442, https://doi.org/10.1103/PhysRevB.79.125442.
[69] M.P. Singh, R.K. Singh, S. Chandra, Studies on Imidazolium-Based Ionic Liquids Having a Large Anion Confined in a Nanoporous Silica Gel Matrix, J. Phys. Chem. B 115 (2011) 7505–7514, https://doi.org/10.1021/jp2003358.
[70] B.D. Hamilton, J.-M. Ha, M.A. Hillmyer, M.D. Ward, Manipulating Crystal Growth and Polymorphism by Confinement in Nanoscale Crystallization Chambers, Acc. Chem. Res. 45 (2012) 414–423, https://doi.org/10.1021/ar200147v.
[71] T. Cordeiro, A.F.M. Santos, G. Nunes, G. Cunha, J.C. Sotomayor, I.M. Fonseca, F. Danède, C.J. Dias, M.M. Cardoso, N.T. Correia, M.T. Viciosa, M. Dionísio, Accessing the Physical State and Molecular Mobility of Naproxen Confined to Nanoporous Silica Matrixes, J. Phys. Chem. C 120 (2016) 14390–14401, https://doi.org/10.1021/acs.jpcc.6b04078.
[72] G. Szklarz, K. Adrjanowicz, M. Tarnacka, J. Pionteck, M. Paluch, Confinement-Induced Changes in the Glassy Dynamics and Crystallization Behavior of Supercooled Fenofibrate, J. Phys. Chem. C 122 (2018) 1384–1395, https://doi.org/10.1021/acs.jpcc.7b10946.
[73] P. Peksa, J. Trzmiel, M. Ptak, M. Kostrzewa, R. Szatanik, A. Barascu, D. Enke, A. Sieradzki, Confinement-induced polymorphism in acetylsalicylic acid–nanoporous glass composites, J. Mater. Sci. 54 (2019) 404–413, https://doi.org/10.1007/s10853-018-2853-8.
[74] Z. Wang, E. Pameté, A. Chojnacka, S.E.M. Pourhosseini, P. Ratajczak, F. Béguin, Effect of oxygenated functionalities on the phase transitions of an ionic liquid confined in a mesoporous carbon host, Carbon. 202 (2023) 571–582, https://doi.org/10.1016/j.carbon.2022.09.049.
[75] N. Zhao, S. Hu, C. Zhang, F. Li, R. Chen, Physical origins of freezing and melting temperature depressions of water in millimeter-sized pores, Colloids Surf. A Physicochem. Eng. Asp. 674 (2023) 131851, https://doi.org/10.1016/j.colsurfa.2023.131851.
[76] H. Bishara, S. Berger, Preferred crystallographic orientation of nanocrystals embedded inside nanopores, Prog. Cryst. Growth Charact. Mater. 65 (2019) 100464, https://doi.org/10.1016/j.pcrysgrow.2019.100464.
[77] M.A. Kolmangadi, L. Zhuoqing, G.J. Smales, B.R. Pauw, E. Wuckert, A. Raab, S. Laschat, P. Huber, A. Schönhals, Confinement-Suppressed Phase Transition and Dynamic Self-Assembly of Ionic Superdiscs in Ordered Nanochannels: Implications for Nanoscale Applications, ACS Appl. Nano Mater. 6 (2023) 15673–15684, https://doi.org/10.1021/acsanm.3c02473.
[78] G.B. McKenna, S.L. Simon, Chapter 2 - The glass transition: Its measurement and underlying physics, in: Handb. Therm. Anal. Calorim., 2002, pp. 49–109, https://doi.org/10.1016/S1573-4374(02)80005-X.
[79] H. Kanno, A simple derivation of the empirical rule $T_G/T_M = 2/3$, J. Non-Cryst. Solids. 44 (1981) 409–413, https://doi.org/10.1016/0022-3093(81)90047-8.
[80] P. Klonos, G. Dapei, I.Y. Sulym, S. Zidropoulos, D. Sternik, A. Deryło-Marczewska, M.V. Borysenko, V.M. Gun'Ko, A. Kyritsis, P. Pissis, Morphology and molecular dynamics investigation of PDMS adsorbed on titania nanoparticles: Effects of polymer molecular weight, Eur. Polym. J. 74 (2016) 64–80, https://doi.org/10.1016/j.eurpolymj.2015.11.010.
[81] W. Tu, K. Jurkiewicz, K. Adrjanowicz, Confinement of pyrrolidinium-based ionic liquids $[C_nMPyrr]^+[Tf_2N]^-$ with long cationic alkyl side chains ($n = 10$ and 16) to nanoscale pores: Dielectric and calorimetric studies, J. Mol. Liq. 324 (2021) 115115, https://doi.org/10.1016/j.molliq.2020.115115.
[82] R. Markiewicz, A. Klimaszyk, M. Jarek, M. Taube, P. Florczak, M. Kempka, Z. Fojud, S. Jurga, Influence of Alkyl Chain Length on Thermal Properties, Structure, and Self-Diffusion Coefficients of Alkyltriethylammonium-Based Ionic Liquids, Int. J. Mol. Sci. 22 (2021) 5935, https://doi.org/10.3390/ijms22115935.
[83] J.C. Dyre, The random free-energy barrier model for ac conduction in disordered solids, J. Appl. Phys. 64 (1988) 2456–2468, https://doi.org/10.1063/1.341681.
[84] J.C. Dyre, T.B. Schrøder, Universality of ac conduction in disordered solids, Rev. Mod. Phys. 72 (2000) 873–892, https://doi.org/10.1103/RevModPhys.72.873.
[85] F. Kremer, S.A. Różański, The Dielectric Properties of Semiconducting Disordered Materials, in: F. Kremer, A. Schönhals (Eds.), Broadband Dielectr. Spectrosc, Springer, Berlin, Germany, 2003, pp. 475–494, https://doi.org/10.1007/978-3-642-56120-7_12.
[86] I. Popov, Z. Zhu, A.R. Young-Gonzales, R.L. Sacci, E. Mamontov, C. Gainaru, S. J. Paddison, A.P. Sokolov, Search for a Grotthuss mechanism through the observation of proton transfer, Commun. Chem. 6 (2023) 77, https://doi.org/10.1038/s42004-023-00878-6.
[87] P. Ben Ishai, M.S. Talary, A. Caduff, E. Levy, Y. Feldman, Electrode polarization in dielectric measurements: A review, Meas. Sci. Technol. 24 (2013) 102001, https://doi.org/10.1088/0957-0233/24/10/102001.
[88] A. Dhahri, E. Dhahri, E.K. Hlil, Electrical conductivity and dielectric behaviour of nanocrystalline $La_{0.6}Gd_{0.1}Sr_{0.3}Mn_{0.75}Si_{0.25}O_3$, RSC Adv. 8 (2018) 9103–9111, https://doi.org/10.1039/c8ra00037a.
[89] O. Oguz, S.A. Koutsoumpis, E. Simsek, E. Yilgor, I. Yilgor, P. Pissis, Y. Z. Menceloglu, Effect of soft segment molecular weight on the glass transition, crystallinity, molecular mobility and segmental dynamics of poly(ethylene oxide) based poly(urethane-urea) copolymers, RSC Adv. 7 (2017) 40745–40754, https://doi.org/10.1039/c7ra08007g.
[90] E.-J. Donth, The Glass Transition: Relaxation Dynamics in Liquids and Disordered Materials, Springer, Berlin Heidelberg, Berlin, Heidelberg (2001), https://doi.org/10.1007/978-3-662-04365-3.
[91] H. Montes-Campos, T. Méndez-Morales, J.M. Otero-Mato, O. Cabeza, L.J. Gallego, E. Lomba, L.M. Varela, Ionic liquids nanoconfined in zeolite-templated carbon: A computational study, J. Mol. Liq. 318 (2020) 114264, https://doi.org/10.1016/j.molliq.2020.114264.
[92] J.M. Otero-Mato, H. Montes-Campos, O. Cabeza, L.J. Gallego, L.M. Varela, Nanoconfined ionic liquids: A computational study, J. Mol. Liq. 320 (2020) 114446, https://doi.org/10.1016/j.molliq.2020.114446.
[93] P.A.M. Steeman, J. van Turnhout, Dielectric Properties of Inhomogeneous Media, in: Broadband Dielectr. Spectrosc, Springer, Berlin, Germany, 2003, pp. 495–522, https://doi.org/10.1007/978-3-642-56120-7_13.
[94] M. Samet, V. Levchenko, G. Boiteux, G. Seytre, A. Kallel, A. Serghei, Electrode polarization vs. Maxwell-Wagner-Sillars interfacial polarization in dielectric spectra of materials: Characteristic frequencies and scaling laws, J. Chem. Phys. 142 (2015) 194703, https://doi.org/10.1063/1.4919877.
[95] G. Pagot, M. Garaga, A.L. Jadhav, L.F. O'Donnell, K. Vezzù, B. Itin, R. J. Messinger, S.G. Greenbaum, V. Di Noto, Interplay between coordination, dynamics, and conductivity mechanism in Mg/Al-catenated ionic liquid electrolytes, J. Power Sources. 524 (2022) 231084, https://doi.org/10.1016/j.jpowsour.2022.231084.
[96] H. Hammami, M. Arous, M. Lagache, A. Kallel, Study of the interfacial MWS relaxation by dielectric spectroscopy in unidirectional PZT fibres/epoxy resin composites, J. Alloys Compd. 430 (2007) 1–8, https://doi.org/10.1016/j.jallcom.2006.04.048.
[97] R. Böhmer, K.L. Ngai, C.A. Angell, D.J. Plazek, Nonexponential relaxations in strong and fragile glass formers, J. Chem. Phys. 99 (1993) 4201–4209, https://doi.org/10.1063/1.466117.
[98] J. Timmermans, Plastic crystals: A historical review, J. Phys. Chem. Solids. 18 (1961) 1–8, https://doi.org/10.1016/0022-3697(61)90076-2.
[99] A. Simonov, A.L. Goodwin, Designing disorder into crystalline materials, Nat. Rev. Chem. 4 (2020) 657–673, https://doi.org/10.1038/s41570-020-00228-3.
[100] D. Cholakova, N. Denkov, Rotator phases in alkane systems: In bulk, surface layers and micro/nano-confinements, Adv. Colloid Interface Sci. 269 (2019) 7–42, https://doi.org/10.1016/j.cis.2019.04.001.
[101] A.-V. Mudring, Solidification of Ionic Liquids: Theory and Techniques, Aust. J. Chem. 63 (2010) 544–564, https://doi.org/10.1071/CH10017.
[102] C. Bin Park, B.J. Sung, Heterogeneous Rotational Dynamics of Imidazolium-Based Organic Ionic Plastic Crystals, J. Phys. Chem. B 124 (2020) 6894–6904, https://doi.org/10.1021/acs.jpcb.0c02433.
[103] S.Y. Chazhengina, E.N. Kotelnikova, I.V. Filippova, S.K. Filatov, Phase transitions of n-alkanes as rotator crystals, J. Mol. Struct. 647 (2003) 243–257, https://doi.org/10.1016/S0022-2860(02)00531-8.
[104] D. Cholakova, K. Tsvetkova, S. Tcholakova, N. Denkov, Rheological properties of rotator and crystalline phases of alkanes, Colloids Surf. A Physicochem. Eng. Asp. 634 (2022) 127926, https://doi.org/10.1016/j.colsurfa.2021.127926.
[105] P. Lunkenheimer, M. Michl, A. Loidl, Nonlinear Dielectric Response of Plastic Crystals, in: Nonlinear Dielectr. Spectrosc, Springer, 2018, pp. 277–300, https://doi.org/10.1007/978-3-319-77574-6_9.
[106] T. Ying, Y. Huang, N. Song, Y. Tan, Y. Tang, Z. Sun, J. Zhuang, X. Dong, Dielectric switching from a high temperature plastic phase transition in two organic salts with chiral features, Mater. Adv. 3 (2022) 1581–1586, https://doi.org/10.1039/d1ma01108a.

[107] S.A. Burrows, E.E. Lin, D. Cholakova, S. Richardson, S.K. Smoukov, Structure of the Hexadecane Rotator Phase: Combination of X-ray Spectra and Molecular Dynamics Simulation, J. Phys. Chem. b. 127 (2023) 7772–7784, https://doi.org/10.1021/acs.jpcb.3c02027.
[108] S.I. Abdul Halim, C.H. Chan, J, Apotheker, Basics of teaching electrochemical impedance spectroscopy of electrolytes for ion-rechargeable batteries - part 1: a good practice on estimation of bulk resistance of solid polymer electrolytes, Chem. Teach. Int. 3 (2021) 105–115, https://doi.org/10.1515/cti-2020-0011.
[109] E. Barsoukov, J.R. Macdonald, Impedance Spectroscopy: Theory, Experiment, and Applications, Wiley (2005), https://doi.org/10.1002/0471716243.
[110] W. Bolton, 12 - Nyquist diagrams, in, Instrum. Control Syst., Newnes (2004) 282–289, https://doi.org/10.1016/B978-075066432-5/50012-7.
[111] B.-A. Mei, O. Munteshari, J. Lau, B. Dunn, L. Pilon, Physical Interpretations of Nyquist Plots for EDLC Electrodes and Devices, J. Phys. Chem. C 122 (2018) 194–206, https://doi.org/10.1021/acs.jpcc.7b10582.
[112] H. Herrera Hernández, A.M. Ruiz Reynoso, J.C. Trinidad González, C.O. González Morán, J.G. Miranda Hernández, A. Mandujano Ruiz, J. Morales Hernández, R. Orozco Cruz. Electrochemical Impedance Spectroscopy (EIS): A Review Study of Basic Aspects of the Corrosion Mechanism Applied to Steels, Electrochem. Impedance Spectrosc., IntechOpen, London, 2020, pp. 1–35, https://doi.org/10.5772/intechopen.94470.
[113] C.M.A. Brett, Electrochemical Impedance Spectroscopy in the Characterisation and Application of Modified Electrodes for Electrochemical Sensors and Biosensors, Molecules 27 (2022) 1497, https://doi.org/10.3390/molecules27051497.
[114] G. Branković, Z. Branković, V.D. Jović, J.A. Varela, Fractal Approach to ac Impedance Spectroscopy Studies of Ceramic Materials, J. Electroceramics. 7 (2001) 89–94, https://doi.org/10.1023/A:1013166204618.
[115] A. Lasia, The Origin of the Constant Phase Element, J. Phys. Chem. Lett. 13 (2022) 580–589, https://doi.org/10.1021/acs.jpclett.1c03782.
[116] N.A. Liedienov, A.V. Pashchenko, V.A. Turchenko, V.Y. Sycheva, A.V. Voznyak, V. P. Kladko, A.I. Gudimenko, D.D. Tatarchuk, Y.V. Didenko, I.V. Fesych, I. I. Makoed, A.T. Kozakov, G.G. Levchenko, Liquid-phase sintered bismuth ferrite multiferroics and their giant dielectric constant, Ceram. Int. 45 (2019) 14873–14879, https://doi.org/10.1016/j.ceramint.2019.04.220.